Analysis of the Effects of Wafer Slicing on the Mechanical Integrity of Silicon Wafers (2010-GIT-4)

Hao Wu, Shreyes N. Melkote, Steven Danyluk
The George W. Woodruff School of Mechanical Engineering
Georgia Institute of Technology, Atlanta, GA, 30332

Abstract

This project aims to provide fundamental understanding of the wire sawing process of silicon wafers. The traditional multi-wire slurry sawing technique (MWSS) and the fixed abrasive diamond wire sawing (DWS) technique as a new promising alternative are compared. Fundamental experimental and modeling studies of single grit diamond scribing on silicon are carried out to derive a first principles understanding of the factors governing the mode of material removal and surface and subsurface damage in diamond wire sawing. Notable progress was achieved in the following areas: (i) comparison of MWSS and DWS, (ii) investigation of the crystallographic orientation dependence of ductile scribing of silicon by taking into account the roles of phase transformation and slip, (iii) understanding the ductile-to-brittle cutting mode transition in single grit diamond scribing of silicon through experiments and extended finite element modeling (XFEM).

1. Analysis of Slurry and Fixed Abrasive Diamond Wire Sawn Silicon Wafers

Various geometric and mechanical characteristics of silicon wafers sliced by slurry and fixed abrasive diamond wire sawing were analyzed through the use of different characterization tools. Specifically, the surface morphology, cutting mode (ductile/brittle), thickness variation, surface roughness, surface profile, residual stresses, microcracks and mechanical strength of multi-Si wafers were examined. In general, diamond cut wafers are found to have characteristics that are comparable to (and in some cases superior to) slurry cut wafers, which indicates that fixed abrasive diamond wire sawing can be a viable alternative to slurry wire sawing [1].

The mechanical strength of silicon wafers cut by both MWSS and DWS was studied in depth through four line and biaxial bending tests [2]. Mixed mode fracture analysis identifies the effect of microcrack geometry on the critical crack length. Microcracks in the wafer edges and center were measured to correlate with the fracture strength of wafers evaluated using linear elastic fracture mechanics. Details of this study can be found in [1, 2], also included in the appendix as A-1 and A-2.

2.Crystallographic Orientation Dependence of Ductile Scribing in Silicon

Single-point diamond scribing tests were performed on (111), (001) and (110) crystallographic planes in the <111>, <110>, <100> and <112> directions. In all cases, the material removal mechanism transitions from ductile to brittle fracture as the depth of scribing increases. The critical depth of ductile-to-brittle transition is found to vary considerably. Scribing on the (001) Si surface exhibits significant brittle fracture, while

ductile removal is achieved on the (111) plane at scribing depths greater than 1μm. In addition, on a given crystallographic plane, brittle fracture is found to always dominate in the <100> direction compared to the <111> direction. These results are explained by the roles of phase transformation and slip generation in the material. For a given scribing depth, orientations for which slip systems are easily activated require higher loading pressures and therefore produce higher tensile stress in the material, which leads to increased brittle fracture. Details can be found in [3], also included in the appendix as A-3.

3. Modeling and Experimental Study on Ductile-to-brittle Cutting Mode Transition in Single Grit Diamond Scribing of Silicon

The effects of scriber tip geometry, coefficient of friction and external hydrostatic pressure on the critical depth of cut associated with ductile-to-brittle transition and crack generation were studied via an eXtended Finite Element Method (XFEM) based model, which was experimentally validated [4, 5]. Scribers with a large tip radius are shown to produce lower tensile stresses and a larger critical depth of cut compared to scribers with a sharp tip. Spherical tipped scribers are shown to generate only surface cracks while sharp tipped scribers (conical, Berkovich and Vickers) are found to create large subsurface tensile stresses, which can lead to nucleation of subsurface median/lateral cracks. Lowering the friction coefficient tends to increase the critical depth of cut and hence the extent of ductile mode cutting. The results also show that larger critical depth of cut can be obtained under external hydrostatic pressure. Details of this study can be found in [4, 5] and is also included in the appendix as A-4.

References

1. Wu, H. et al., "Analysis of Slurry and Fixed Abrasive Diamond Wire Sawn Silicon Wafers*", 21th Workshop on Crystalline Silicon Solar Cells & Modules: Materials and Processes***,** Breckenridge, CO, USA, 2011
2. Wu, H., Melkote, S. N. and Danyluk, S., *"*Mechanical Strength of Silicon Wafers Cut by Loose Abrasive Slurry and Fixed Abrasive Diamond Wire Sawing*"*, in press, *Advanced Engineering Materials.*
3. Wu, H. and Melkote, S.N., *"*Effect of Crystallographic Orientation on Ductile Scribing of Crystalline Silicon Role of Phase Transformation and Slip*"*, under review, *Materials Science and Engineering: A.*
4. Wu, H. and Melkote, S.N., "Modeling and Experimental Study on Ductile-to-Brittle Cutting Mode Transition in Single Grit Diamond Scribing of Silicon: Application to Wire Sawing of Silicon Wafers," *26th European Photovoltaic Solar Energy Conference and Exhibition*, Hamburg, Germany, September 2011, pp. 966-970.
5. Wu, H. and Melkote, S.N., "Study of Ductile-to-Brittle Transition in Single Grit Diamond Scribing of Silicon: Application to Wire Sawing of Silicon Wafers*",* under review, *Journal of Engineering Materials & Technology, ASME Transactions.*

Appendix A-1: Presented at the 2011 Crystalline Silicon Workshop
Breckenridge, CO

Analysis of Slurry and Fixed Abrasive Diamond Wire Sawn Silicon Wafers

Hao Wu, Kevin Skenes, Chris Yang, Frank Mess, Shreyes N. Melkote, Steven Danyluk
The George W. Woodruff School of Mechanical Engineering
Georgia Institute of Technology, Atlanta, GA, 30332

Abstract

Various geometric and mechanical characteristics of silicon wafers sliced by slurry and fixed abrasive diamond wire sawing are analyzed through measurements. In general, diamond cut wafers are found to have comparable characteristics as slurry cut wafers, which indicates that fixed abrasive diamond wire sawing may be a viable alternative to slurry wire sawing.

1. Introduction

While slurry based wire sawing is currently the prevalent process technology to manufacture photovoltaic silicon wafers [1], fixed abrasive diamond wire sawing is a promising new technology due to its potential for high throughput and possible ease of recycling cutting fluid and silicon [2-4]. The objective of this study is to quantitatively analyze and compare the characteristics of silicon wafers sliced by the two techniques.

As-cut 156mm square polycrystalline Si wafers produced by the two sawing techniques were provided by two industrial vendors (denoted as A and B) and are summarized in Table 1. The surface morphology, cutting mode (ductile/brittle), thickness variation, surface roughness, surface profile, residual stresses, microcracks and mechanical strength of the Si wafers are examined, followed by discussion of the key results.

Table 1. Si wafers used in this study

Vendor A			**Vendor B**	
Diamond cut (VAD)	Slurry cut group 1 (VAS1)	Slurry cut group 2 (VAS2)	Diamond cut (VBD)	Slurry cut (VBS)
200 µm thick	160 µm thick F600 cutting grit	160-200 µm thick F800 cutting grit	200 µm thick	200 µm thick

2. Results

2.1 Surface Morphology and Cutting Mode

It has been shown that slurry cut wafers typically exhibit a rough surface with random texture, whereas diamond cut wafers typically have smooth cutting grooves along the cutting direction [4]. As seen in Fig.1, there is also some brittle chipping along the smooth cutting traces. It is known that diamond cubic silicon, when subjected to very high pressures (>8GPa), undergoes phase transformation resulting in new crystalline phases (e.g. Si-III, Si-XII) at low unloading rates, or amorphous silicon at high unloading rates [5]. It is believed that the ductile cutting mode of silicon is due to formation of the amorphous phase [6]. The Raman spectra in Fig. 2 indicates the presence of amorphous silicon in the smooth cutting grooves of the diamond cut wafers. In general, amorphous silicon is observed in the ductile cutting regions of diamond cut wafers while it is rarely observed in slurry cut wafers, whose

surfaces mostly exhibit the diamond cubic phase.

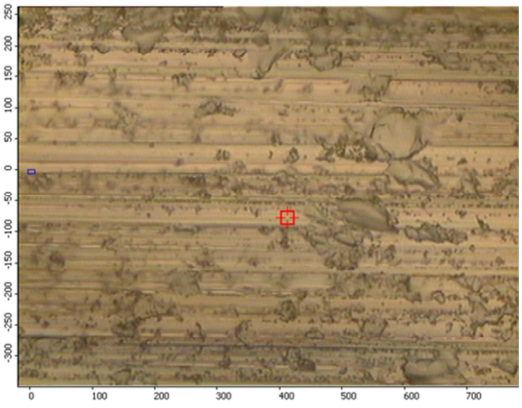

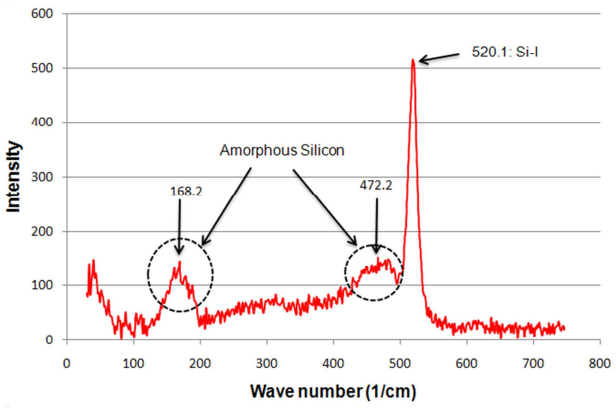

Fig. 1. Image of diamond cut wafer surface (VAD). Fig. 2. Raman spectra of marked region in Fig. 1

2.2 Thickness Variation

The thickness of slurry cut wafers was observed to vary as a function of location in the wafer. Specifically, along the wire speed direction (see Fig. 3) the right edge (T2,T4) is generally thicker than the left edge (T1,T3), and along the wire feed direction the bottom edge (T3,T4) is thicker than the top edge (T1,T2). The thickness variation as a function of wafer location is shown in Fig. 4. In contrast, the diamond cut wafers showed random thickness variation of about 20µm.

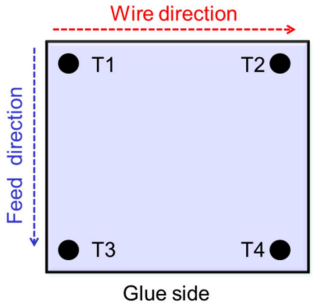

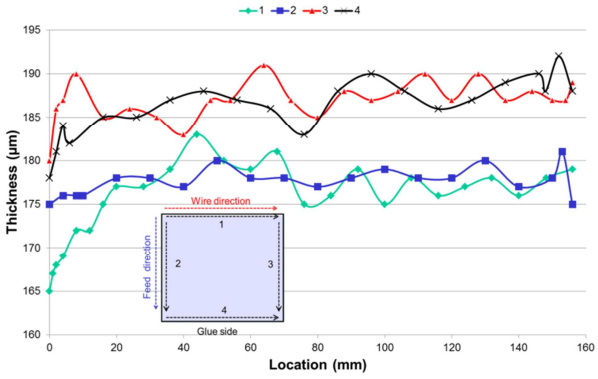

Fig. 3. Wafer cutting schematic. Fig. 4. Slurry cut wafer thickness variation.

2.3 Surface Roughness

Figure 5 shows the surface roughness variation along the wire speed direction measured using an optical Interferometer. The roughness of slurry cut wafers decreases significantly from wire entry (left edge) to exit (right edge). However, the roughness remains nearly constant along the wire feed direction. In contrast, the measured roughness of the diamond cut wafers appears to depend on local cutting conditions and can have large random variations, especially when measured along the wire speed direction.

2.4 Surface Profile

The wafer surface profiles were measured using a Taylor Hobson Talysurf® profilometer

along a 100mm track perpendicular to the saw marks in the wafer center. Both the back and front wafer surface profiles were measured. Representative profiles of slurry and diamond cut wafers are shown in Fig. 6. Note that the back surface profiles are plotted such that the difference between the back and front surface profiles represents the thickness variation. It can be seen that, in general, diamond cut wafers have larger surface profile variation. There appears to be a strong correlation between the profile variation between the back and front surfaces of both slurry and diamond cut wafers. This may be due to the synchronous displacement of the ganged cutting wires. Note also that slurry cut wafers exhibit smaller thickness variation than diamond cut wafers.

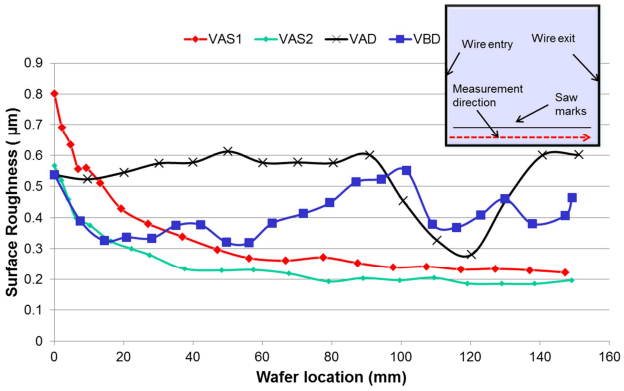

Fig. 5. Surface roughness as a function of location.

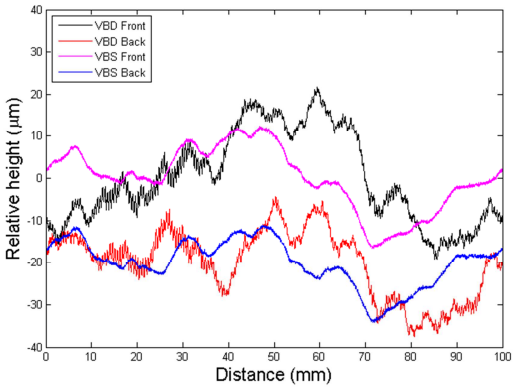

Fig. 6. Surface profile measurement.

2.5 Residual Stress

The maximum in-plane shear residual stresses in the wafers from the each group provided by Vendor A were analyzed using a near-infrared circular polariscope. The six-step phase stepping method proposed by Patterson and Wang [7] was used to solve for the phase retardation and isoclinic angle of the infrared light passing through the sample, which were then used to calculate the maximum shear stress τ_{max} via the stress-optic law [8]. The average maximum shear stresses for wafer groups VAS1 and VAS2 were observed to be in the range 1.5 – 3.3 MPa, whereas the VAD group yielded an average value of 2.4 MPa (see Fig. 7). The diamond cut wafers reveal a noticeable vertical stress pattern along the wire feed direction.

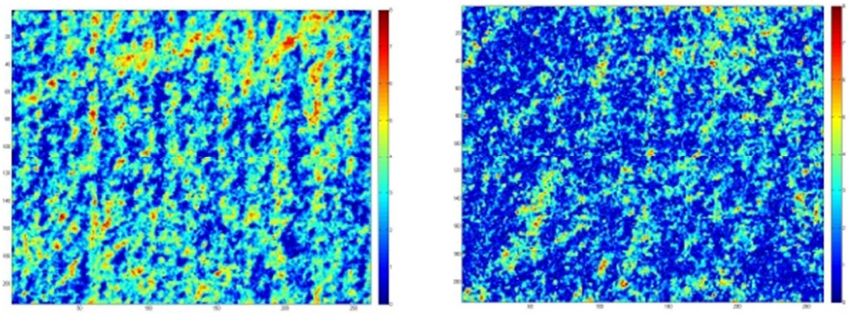

Fig. 7. τ_{max} in VAD wafer (left) and VAS2 wafer (right); each figure represents a 225 mm^2 section of the wafer.

2.6 Microcracks

The presence of microcracks in the wafer subsurface determines its fracture. Selected wafer

edges were polished to directly observe and measure microcrack distributions. These measurements were carried out for wafers of different cutting conditions, and the results are summarized in Table 2. The crack density refers to the number of observed cracks per unit length of the wafer edge. Measured crack lengths for polished wafer edges were found to fit the Weibull distribution quite well. It is of particular interest that the crack density of diamond cut wafers is approximately twice that of slurry cut wafers, while the expected crack length of diamond cut wafers, derived from the Weibull analysis, is smaller than for the slurry cut wafers.

Table 2. Summary of wafer edge crack measurement

	VAD	VAS1	VAS2	VBD	VBS
Crack Density (/mm/edge)	19.0	7.7	6.7	21.4	11.5
Max Length (μm)	8.5	10.3	7.8	6.3	9.7
Expected Length (μm)	3.0	4.8	3.3	2.5	4.4
Standard Deviation (μm)	1.2	2.2	1.0	1.0	1.6

2.7 Fracture Strength

The fracture strength of both slurry and diamond cut wafers were determined using four line bending tests. Figure 8 shows a Weibull plot of the fracture strength data. It can be seen that diamond cut wafers have fracture strengths comparable to the slurry cut wafers, although they exhibit larger variation. One group of diamond cut wafers (VBD) yielded significantly higher fracture strength than the other wafer groups. As expected, slurry cut wafers produced by a larger grit size wire (VAS1, F600) have lower fracture strengths than those produced by a smaller grit size wire (VAS2, F800).

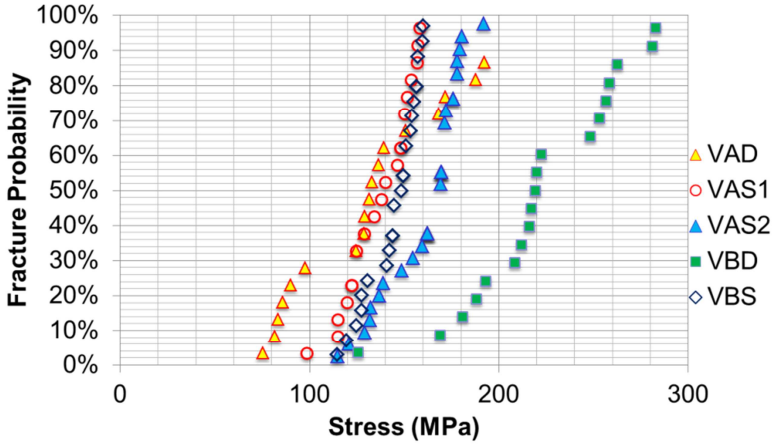

Fig. 8. Four line bending fracture probability.

3. Discussion

Material removal in slurry sawing of Si wafers is fundamentally due to three body abrasion between the wire, cutting grits (typically silicon carbide), and silicon ingot in the presence of a cutting fluid. On the other hand, diamond wire sawing is primarily due to two-body abrasion (or scratching) between the diamond grits embedded in the cutting wire and the silicon ingot in the presence of a cutting fluid. The ductile mode cutting grooves (saw marks) observed on diamond cut wafers (see Fig. 1) are generated by two-body abrasion.

The variation in wafer thickness and surface roughness observed in slurry cut wafers is attributed to the complex interaction of the wire, abrasive and silicon ingot. For slurry cut wafers, it is believed that the cutting action during wire entry is dominated by the large grits in the slurry while the smaller grits are entrained in the slurry and play a smaller role in the material removal process. The larger grits lead to a rougher surface and wider kerf (thus thinner wafer) where the wire enters the ingot. As the wire moves through the ingot, the larger grits tend to fragment because of their friability and a greater number of smaller grits begin to participate in three-body abrasion leading to lower surface roughness and smaller kerf width (i.e. thicker wafer) at wire exit. In the two-body cutting mechanism of diamond wire sawing, hydrodynamic forces play a lesser role, and cutting is achieved by the scratching action of the diamond grits of random shape and size embedded in the steel wire. Therefore variations in thickness and roughness tend to be generally more random.

Fixed abrasive diamond-cut wafers have larger crack density than slurry-cut wafers. However, the mean crack length estimated from the Weibull analysis is smaller for diamond-cut wafers than for slurry-cut wafers. Meanwhile, diamond cut wafers exhibit fracture strengths that are comparable to slurry-cut wafers.

These results suggest that fixed abrasive diamond wire sawing of silicon ingots can be a viable alternative to slurry sawing from the standpoint of wafer production. Coupled with higher throughput, this may make fixed abrasive diamond wire sawing the process of choice in the future. Prior to the use of fixed abrasive cutting systems in production, additional investigation is required for the effective removal of the amorphous Si layer produced by ductile mode of cutting. This might be achieved by changing etching protocol or increasing etching time [9].

4. Acknowledgements

The authors thank Jose Cariaga of REC (Norway) and Mike Seacrist (MEMC) for providing the wafers used in this study. Financial support of the NSF Silicon Solar Consortium (SiSoC) is also gratefully acknowledged.

5. References

1. Moller HJ., *Phys. Stat. Sol.* (a) 2006; **203**(4): 659-669
2. Kondo Y, et al., *Proceedings of the 23rd EUPVSEC*, Valencia, 2008: 1297
3. Watanabe N, et al., *Prog. Photovolt: Res. Appl.* 2010; **18**: 485-490
4. Bidiville A, et al., *Proceedings of the 24th EUPVSEC, Hamburg*, 2009: 2CV.1.86
5. Morris JC and Callahan DL, *J. Mater. Res.*, 1994. **9**(11): p. 2907- 2913.
6. Kailer, A., et al., *J. Appl. Phys*, 1997. **81**(7): p. 3057-3063
7. E. A. Patterson and Z. F. Wang, *Strain*, 1991; **27:** 27-49
8. He SJ, Zheng T, Danyluk, *J. Appl. Phys*, 2004. **96**(6): p. 3103-3109
9. Holt A, et al., *Proceedings of the 35th IEEE PVSC*, Honolulu, HI, 2010: 003501 – 003504

ADVANCED ENGINEERING MATERIALS

DOI: 10.1002/adem.201100263

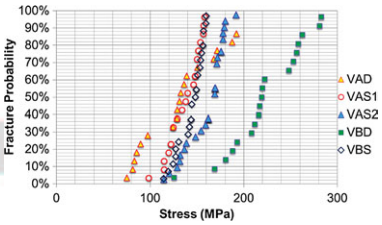

Mechanical Strength of Silicon Wafers Cut by Loose Abrasive Slurry and Fixed Abrasive Diamond Wire Sawing

H. Wu, S. N. Melkote, S. Danyluk*

Mechanical strength of silicon wafers cut by loose and fixed abrasive diamond wire sawing techniques are studied through four line and biaxial bending tests. Mixed mode fracture analysis identifies the effect of microcrack geometry on the critical crack length. Microcracks in the wafer edges and center are measured to correlate with the fracture strength of wafers evaluated using linear elastic fracture mechanics.

ADV. ENG. MATER. 2011, 00 . . . . . xx–xx

ADVANCED ENGINEERING MATERIALS

DOI: 10.1002/adem.201100263

Mechanical Strength of Silicon Wafers Cut by Loose Abrasive Slurry and Fixed Abrasive Diamond Wire Sawing

By *Hao Wu, Shreyes N. Melkote** and *Steven Danyluk*

This paper reports on the mechanical strength of polycrystalline silicon wafers cut by loose abrasive slurry and fixed abrasive diamond wire sawing processes. Four line bending and biaxial flexure tests are used to evaluate the fracture strength of the wafers. Fracture strength of the wafers depends on the location, size, and orientation of microcracks in the silicon wafer and the distribution and magnitude of applied stresses. Measurement of microcracks at the wafer edge and center shows that edge cracks are typically larger than center cracks. Fixed abrasive diamond wire sawn wafers are found to have a higher crack density but smaller average crack length. Wafer fracture in four line bending is found to be primarily due to the propagation of edge cracks while center cracks are found to be the primary cause of wafer failure in biaxial flexure tests. Fracture mechanics based analyses demonstrate that crack orientation plays a significant role in four line bending, but not in biaxial flexure. Correlations of the wafer fracture strength and critical crack length agree well with microcrack measurements. The fracture strength of diamond cut wafers is found to be comparable or superior to the strength of slurry cut wafers.

Crystalline silicon (Si) based solar cells continue to be dominant in the photovoltaic (PV) market and a good deal of effort has been expended in lowering the manufacturing costs of cells and modules. A significant portion of this cost is attributable to the silicon with 60% of the Si solar cell costs related to the wafer itself.[1] The mechanical integrity of the Si wafers is of considerable importance in the solar cell production process since fracture during processing can raise the costs significantly. Si is a brittle material and its breakage occurs by elastic fracture.[2] With increasing use of thinner wafers to lower material costs,[3] wafer breakage due to fracture during handling and processing of solar cells is a major issue.

Wafer breakage is believed to be related to microcracks created in the sawing operation. While loose abrasive slurry based wire sawing is currently the mainstream technology for producing PV silicon wafers,[4–6] fixed abrasive diamond wire sawing is rapidly gaining importance due to its potential for high productivity.[7–9] However, there are few studies that discuss the mechanical characteristics of diamond cut wafers relative to slurry cut wafers. Our objective was to compare the mechanical strengths of polycrystalline silicon wafers cut by both loose abrasive slurry and diamond wire sawing methods and evaluate the differences in wafer strengths obtained using two different wafer bending tests, namely, four line bending and biaxial flexure.

Fundamentally, breakage of Si wafers is due to the presence of microcracks in the wafer and applied stresses arising from wafer handling/processing operations that exceed a critical value necessary for wafer failure.[10] Knowledge of the microcrack population, location, and geometry as well as the distribution of applied stresses is required to predict and/or prevent wafer breakage. It is believed that microcracks extend from the wafer surface into the material and have a typical length of up to 10–15 μm while edge cracks are usually longer.[1] However, no statistical measurement of crack lengths exists to prove/disprove the foregoing belief. Monte Carlo simulation was employed by Rupnowski and Sopori[11] to investigate the fracture strength of Si wafers with surface, edge and bulk flaws under uniaxial tensile stresses.[11] However, the actual stress state during wafer/cell processing and handling is more complex than uniaxial tension. Additionally, there are nonlinear effects arising from large wafer deflection, especially for thin wafers, that impact the stress state and hence wafer fracture.

In order to avoid the complexity in stress analysis, Si wafer strength is typically evaluated by standard bending tests.[12]

[*] *H. Wu, Prof. S. N. Melkote, Prof. S. Danyluk*
The George W. Woodruff School of Mechanical Engineering, Georgia Institute of Technology, Atlanta, GA 30332, USA
E-mail: shreyes.melkote@me.gatech.edu

Four-line bending, which generates uniform stresses in the wafer between the lines of load application, is sensitive to edge cracks because it is usually the longer cracks on the edge that lead to wafer breakage. The biaxial flexure strength test eliminates the influence of edge cracks by producing the largest stress in the wafer center while the edges are almost stress free. Therefore, wafer breakage in the biaxial test typically results from the propagation of cracks in the wafer center.

In this paper, four line bending and biaxial flexure tests are used to evaluate the strength of multicrystalline Si wafers produced by loose abrasive slurry and fixed abrasive diamond wire sawing processes, as well as to establish the effect of edge cracks (in the four line test) and center cracks (in the biaxial test) on the mechanical strength of similarly cut wafers. In order to achieve this goal, the typical statistics of microcracks generated by the two wafer cutting processes are established through measurement.

1. Measurement of Microcracks

Multicrystalline Si PV wafers of $156 \times 156\,mm^2$ produced by the two wire sawing methods were obtained from two industrial vendors (denoted by A and B). The samples from Vendor A include one group of 200 μm thick wafers cut by diamond wire sawing and two groups of slurry cut wafers (160–200 μm thick) produced from different cutting grit sizes. The cutting grit size distributions used for the slurry cut wafers follow the powder size specifications of the Federation of European Producers of Abrasive Products (FEPA) and were F600 and F800, respectively. In this paper, diamond cut wafers from vendor A are denoted by the symbol VAD, while slurry cut wafer groups from the same vendor are denoted by VAS1 (F600 wafers) and VAS2 (F800 wafers). The diamond and slurry cut wafers from vendor B (both 200 μm thick) are denoted as VBD and VBS, respectively.

Knowledge of microcrack density, length, and geometry is essential for evaluating the wafer strength. In this study, microcracks at the wafer edge and subsurface cracks in the wafer center were measured under an optical microscope after polishing of the wafer cross-section. Specifically, a small portion of the wafer edge of interest was polished to observe the edge cracks. For center cracks, a small portion of the center of the Si wafer was cut and used. The piece of Si containing the region of interest (wafer edge or center) was sandwiched between two rigid PVC blocks that serve as a fixture during polishing. The sandwiched wafer edge and PVC block assembly was then polished on a Logitech® PM5 polisher using colloidal silica suspension of 60 nm nominal grit size. Polishing was carried out till microcracks in the polished cross-section were observed when viewed in a Keyence® VHX-600 digital optical microscope. A representative image of the polished surface of the wafer edge indicating edge cracks is shown in Figure 1.

Edges of wafers of each type were polished using the procedure described above and the number of cracks in a fixed length of the wafer edge were counted and their lengths measured. At least 200 cracks were counted in each case thereby yielding a sufficiently large sample size for statistical analysis. Microcracks less than 1 μm in length were not counted as they were assumed to not play a major role in determining the wafer fracture strength. The distribution of crack length L thus obtained was fitted to the Weibull distribution[13] as follows:

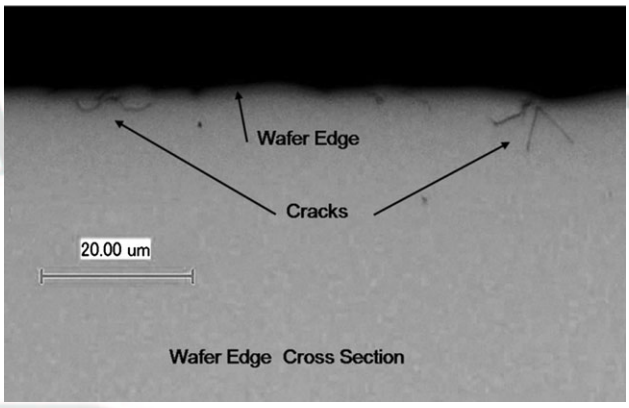

Fig. 1. Edge cracks in VAD wafer.

$$L(l) = \frac{k}{\lambda}\left(\frac{l}{\lambda}\right)^{k-1} e^{-(l/\lambda)^k} \quad (1)$$

where l is the measured crack length, k is the shape parameter, and λ is the scale parameter. Figure 2 shows a comparison of the fitted crack length distribution and measured data for VBS wafers.

The Weibull distribution has an expected value (or mean) given by

$$E(l) = \frac{1}{\lambda}\Gamma\left(1+\frac{1}{k}\right) \quad (2)$$

and a variance given by

$$\mathrm{Var}(l) = \frac{1}{\lambda^2}\left\{\Gamma\left(1+\frac{2}{k}\right) - \Gamma\left(1+\frac{1}{k}\right)^2\right\} \quad (3)$$

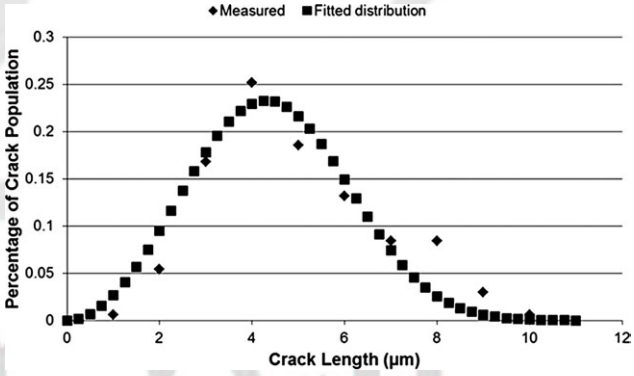

Fig. 2. Representative fit of the Weibull distribution to the measured crack lengths for VBS wafers.

Table 1. Wafer edge crack measurement summary.

	VAD	VBD	VAS1	VAS2	VBS
Crack density [/mm/edge]	19.0	21.4	7.7	6.7	11.5
Max length [μm]	8.5	6.3	10.3	7.8	9.7
Expected length [μm]	3.0	2.5	4.8	3.3	4.4
Standard deviation [μm]	1.2	1.0	2.2	1.0	1.6

where $\Gamma()$ is the gamma function. The crack length measurements and data fitting were carried out for both slurry cut and diamond cut wafers and the results are summarized in Table 1.

In the table, crack density refers to the number of microcracks per millimeter of wafer edge. It can be seen that the crack density in diamond cut wafers is approximately twice that in slurry cut wafers, while the expected crack length for diamond cut wafers is smaller than for slurry cut wafers. Since longer cracks are more likely to cause wafer breakage, the maximum crack length is also listed for comparison. Note that the maximum crack length does not represent the maximum crack length in the entire wafer but only in the section of the wafer edge analyzed.

Microcracks in the wafer center were also measured. Wafers were cut through the center, and the edges produced were polished as before to reveal subsurface microcracks. These results are summarized in Table 2.

It can be seen from the tables that the crack density and the expected length of center cracks are smaller than for edge cracks. This may be due to the different geometric boundary conditions present during sawing of the wafer edges compared to sawing the wafer center. Moreover, before wire sawing, the multicrystalline Si ingots are ground, which can also induce microcracks in the wafer edges. Note that diamond cut wafers have larger crack density and shorter expected crack length than the slurry cut wafers.

2. Wafer Strength Evaluation

The fracture strength of wafers produced by the two sawing processes was evaluated using four line bending and biaxial flexure tests. Results of these tests are presented next.

2.1. Four Line Bending

Four line bending generates maximum stress on the back surface of the sample in the region between the two load application lines. Because the edge crack length is greater than the length of cracks in the wafer center, an edge crack propagates at a lower stress level and consequently the four line bending test is ideal for studying the effect of edge cracks on the fracture strength.[11,14] Based on the small-strain linear elastic theory, which is commonly used in the literature, the maximum tensile stress generated in the wafer during four line bending is calculated as follows:

$$\sigma_m = \frac{3F(L-l)}{2dt^2} \quad (4)$$

where F is the applied load, l and L are the distances between the upper and lower load application lines, d is the wafer width, and t is the wafer thickness. However, it is observed that the deflection of Si wafers prior to breakage can be in excess of 10 mm. The large elastic deformation of the wafer invalidates the small-strain linear elastic theory and necessitates the use of nonlinear large strain elastic theory to accurately determine the wafer stresses.

Figure 3 shows a comparison of the maximum tensile stress calculated using the small-strain linear model in Eq. (4) and a large strain model solved using the finite element method (FEM). It can be seen that as the applied force increases, the resultant nonlinearity can lead to stress discrepancies as large as 50 MPa. Therefore, nonlinear FEM models are used in this study to analyze the fracture strength.

The typical maximum principal stress distribution in the wafer computed using the nonlinear model is shown in Figure 4. As expected, large tensile stresses occur between the two lines of load application. Due to the large deflection and contact between the loading lines and the wafer, the wafer edges experience the largest stress, thereby increasing the probability of wafer failure due to propagation of edge cracks.

As noted earlier, wafer breakage occurs due to the existence of microcracks and applied stresses. According to Linear Elastic Fracture Mechanics (LEFM), a crack will propagate if the stress intensity factor exceeds the fracture toughness of the material[15]:

$$K_{(I,II)} = Y\sigma\sqrt{\pi a} \geq K_{(I,II)c} \quad (5)$$

where σ is the applied stress, a is the crack length, and Y is a dimensionless constant that depends on crack geometry and the loading mode; K_I and K_{II} are the stress intensity factors for

Table 2. Wafer center crack measurement summary.

	VAD	VBD	VAS1	VAS2	VBS
Crack density [/mm/edge]	15.0	17.3	6.6	4.9	8.9
Max. length [μm]	5.0	5.4	5.6	5.3	5.5
Expected length [μm]	2.2	2.2	3.1	2.4	3.0
Standard deviation [μm]	0.7	0.7	0.8	0.9	1.0

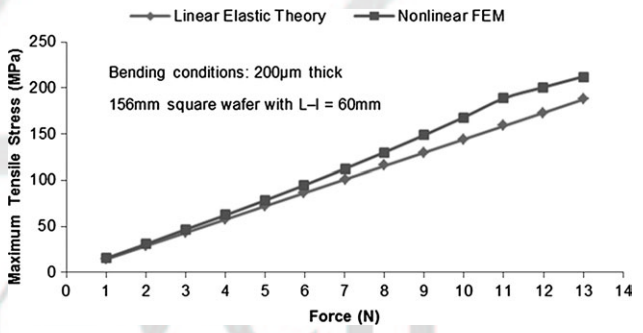

Fig. 3. Comparison of linear and nonlinear elastic models for calculating the tensile stress produced in the wafer.

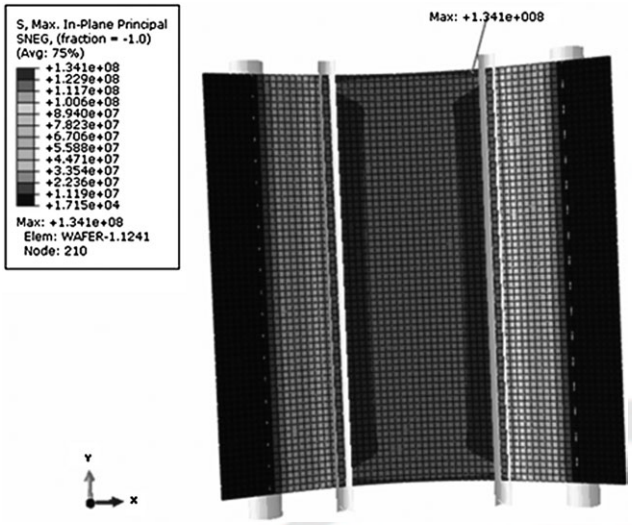

Fig. 4. Maximum principal stress distribution in four line bending.

mode I (crack opening mode) and mode II (in-plane shear mode) failure. Note that for thin Si wafers the out-of-plane stress is negligible and therefore mode III failure (out-of-plane shear) is not considered.

It is evident from Equation 5 that crack length plays a significant role in determining the fracture strength. Meanwhile, the geometry/orientation of the cracks determines Y, which has a significant effect when both fracture modes are in effect as discussed next section.

Since the length of a microcrack is much smaller than the wafer thickness, the wafer edge can be assumed to be in uniaxial tension, as indicated by the FEM results.

An angled crack on the wafer edge is shown in Figure 5. When $\beta \neq 0$, both mode I and mode II failures take place and the stress intensity factors are given by[15]:

$$K_I = K_{I(0)}\cos^2\beta \tag{6}$$

$$K_{II} = K_{I(0)}\cos\beta\sin\beta \tag{7}$$

Suppose the crack propagates at an angle α from the crack plane, the local Mode I and Mode II stress intensity factors at the crack tip are given by[15]:

$$k_I(\alpha) = C_{11}K_I + C_{12}K_{II} \tag{8}$$

$$k_{II}(\alpha) = C_{21}K_I + C_{12}K_{II} \tag{9}$$

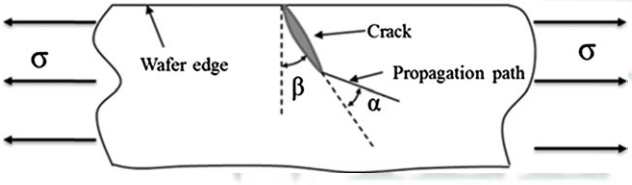

Fig. 5. Angled wafer edge crack.

where the coefficients are given by

$$C_{11} = \frac{3}{4}\cos\left(\frac{\alpha}{2}\right) + \frac{1}{4}\cos\left(\frac{3\alpha}{2}\right) \tag{10}$$

$$C_{12} = -\frac{3}{4}\left[\sin\left(\frac{\alpha}{2}\right) + \sin\left(\frac{3\alpha}{2}\right)\right] \tag{11}$$

$$C_{21} = \frac{1}{4}\left[\sin\left(\frac{\alpha}{2}\right) + \sin\left(\frac{3\alpha}{2}\right)\right] \tag{12}$$

$$C_{22} = \frac{1}{4}\cos\left(\frac{\alpha}{2}\right) + \frac{3}{4}\cos\left(\frac{3\alpha}{2}\right) \tag{13}$$

The crack will propagate if the energy release rate exceeds the fracture toughness:

$$G(\alpha) = \frac{k_I^2(\alpha) + k_{II}^2(\alpha)}{E} \geq G_c \tag{14}$$

By maximizing $G(\alpha)$ for a given orientation β, the crack propagation direction α^* can be determined.

For a given crack propagation direction, the critical crack length for a given applied stress can be calculated based on the energy release rate principle. Critical crack length ratio $a_{c\beta}/a_{c0}$ is defined as the ratio of the critical length of an angled crack with orientation β divided by the critical length of a pure mode I crack ($\beta = 0$) for the same applied stress. Figure 6 shows that for $\beta < 40^\circ$ the angle does not have a significant effect on the critical crack length. Cracks with an orientation of $\beta = 21.9^\circ$ are easiest to propagate with a minimum critical crack length ratio of 0.94.

Wafer breakage tests were carried out for wafers from different sawing conditions. The Weibull distribution, which is commonly used for the analysis of fracture of brittle materials,[16] describes the probability of fracture at a given

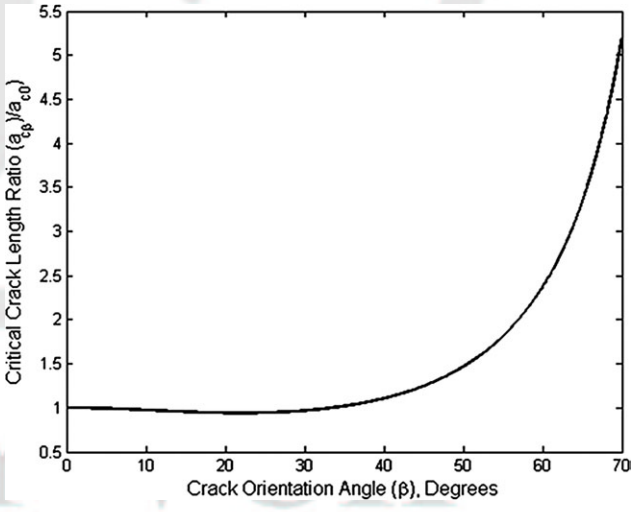

Fig. 6. Critical crack length ratio in four line bending.

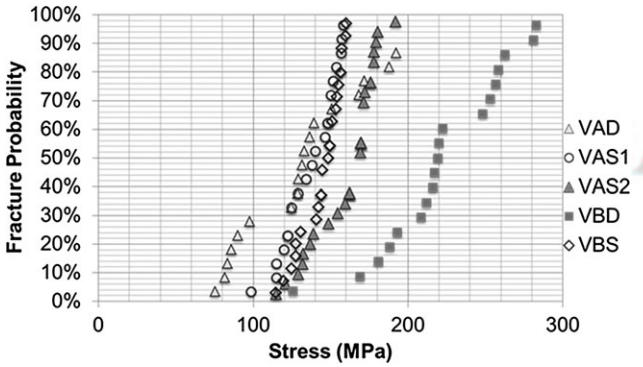

Fig. 7. Weibull plots for wafer fracture strength in four line bending.

stress level as:

$$P_f = 1 - \exp\left[-\left(\frac{\sigma}{\sigma_\theta}\right)^m\right] \quad (15)$$

where σ is the fracture stress, σ_θ is the characteristic stress at which the probability of fracture is 63.2%; the Weibull modulus, m, describes the strength distribution (higher the value of m, lower the strength variability).[17] Figure 7 shows the Weibull plots for the wafer groups examined in this study.

It can be seen that diamond cut wafers have fracture strengths that are at least comparable to slurry cut wafers, although they exhibit larger variation. Note that one group of diamond cut wafers (VBD) has a much higher fracture strength than the others and may have a bimodal fracture probability. Note also that slurry cut wafers sawn using a larger grit size (VAS1, F600) yield a smaller fracture strength than those cut with a smaller grit size (VAS2, F800).

From the LEFM theory, assuming the edge crack to be a quarter-circular crack in a quarter-infinite body, the mode I stress intensity factor under a far-field tensile stress σ is given by[18]:

$$K_I = 1.2735\sigma\sqrt{\pi a} \quad (16)$$

The corresponding critical crack length under tensile loading is then given by:

$$a_c = \frac{1}{\pi}\left(\frac{1.2735\sigma_f}{K_{IC}}\right)^2 \quad (17)$$

where σ_f is the fracture strength and K_{IC} is the mode I fracture toughness. In the four line bending case, due to the fact that edge cracks are longer and the tensile stresses in the large stress region are almost of the same magnitude, wafer breakage is due to the propagation of an edge crack with length equal to the critical crack length.

The mode I fracture toughness of multicrystalline silicon reported in the literature has relatively large variation (0.86–1.1 MPa $\sqrt{m}$).[19–21] Using fracture toughness values ranging from 0.86–1.1 MPa $\sqrt{m}$ and the four line bending fracture strengths, the corresponding mode I critical crack lengths a_c were estimated and are given in Table 3. The largest measured crack length is also listed for comparison.

Table 3. Fracture strength vs. critical crack length in four line bending.

	VAD	VBD	VAS1	VAS2	VBS
Expected fracture stress [MPa]	136.2	221.7	136.4	160.4	143.9
Calculated mode I a_c [μm] (LEFM)	7.8–12.8	3.0–4.8	7.8–12.8	5.6–9.2	7.0–11.5
Measured largest edge crack length [μm]	8.5	6.3	10.3	7.8	9.7

It can be seen that the measured data is in good agreement with the predicted critical crack lengths. However, caution should be exercised in making the comparison for three reasons. First, the measured cracks are not necessarily those which lead to fracture, although they are from the same sawing condition and are therefore supposed to follow the same statistics. Second, in addition to crack length, the crack orientation also plays an important role in wafer failure. Finally, the occurrence of the largest crack in the measurements reported here is a stochastic process. Nevertheless, the measured maximum crack length can still be used as a rough estimate for calculating the wafer fracture strength.

2.2. Biaxial Flexure

In order to eliminate the effect of wafer edges on the fracture strength, the biaxial flexure test, which was originally designed for evaluating the strength of ceramics (ASTM F394-74T),[22] was used to evaluate the mechanical strength of some of the slurry cut Si wafers.[23] The design of the setup is similar to that reported elsewhere.[24]

Due to the large deflection, complex loading and boundary conditions, nonlinear FEM modeling is used to compute the stresses in this test. A representative maximum principal stress distribution in the wafer back surface is shown in Figure 8.

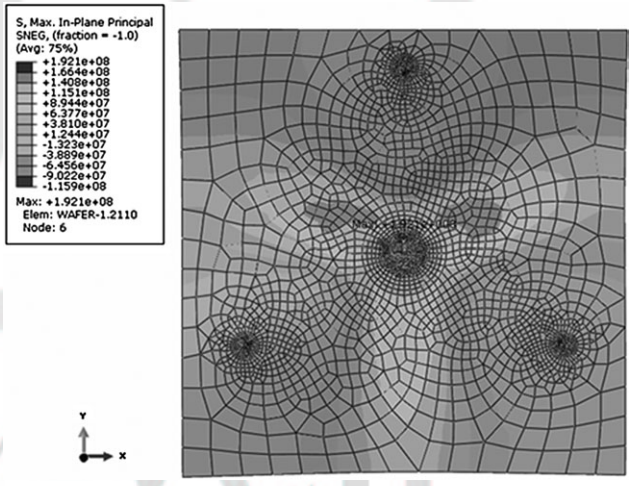

Fig. 8. Maximum in-plane principal stress distribution in wafer back surface during biaxial bending.

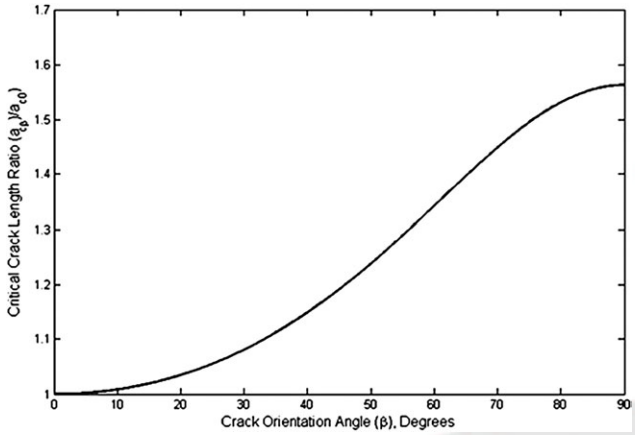

Fig. 9. Critical crack length ratio for angled cracks in biaxial flexure.

In the biaxial test, the largest stress area is subject to principal stresses σ_1 and σ_2, where σ_1 is greater than σ_2. For an angled crack under biaxial loading, the mixed mode stress intensity factors are given by[15]:

$$K_I = K_{I(0)}\left(\cos^2\beta + B\sin^2\beta\right) \quad (18)$$

$$K_{II} = K_{I(0)}\cos\beta\sin\beta(1-B) \quad (19)$$

Note that $B = 0.8$ in this study. Following mixed mode fracture analysis, the critical crack length ratio $a_{c\beta}/a_{c0}$ for angled cracks is shown in Figure 9. Unlike four line bending, the crack orientation does not have a significant effect on the critical crack length as the maximum critical crack length ratio is less than 1.6 at $\beta = 90^\circ$.

Biaxial fracture tests were carried out on only the VAS1 and VAS2 wafers in order to compare the fracture strengths obtained in the two testing approaches. Weibull plots of the results are shown in Figure 10. It can be seen that the biaxial fracture strength is greater than the four line fracture strength for wafers of the same cutting condition. Also, for the same testing conditions, the fracture strength of VAS1 is always less than VAS2.

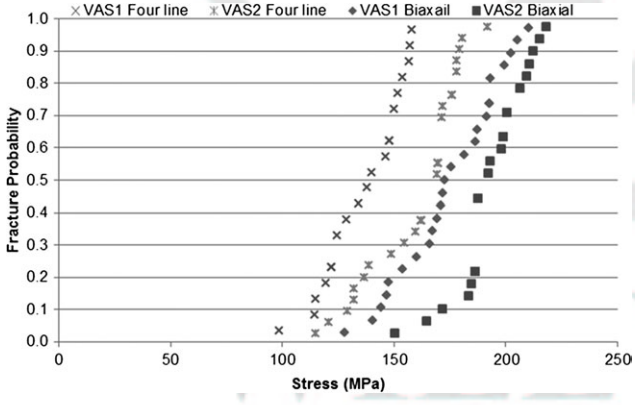

Fig. 10. Weibull plots for both four line and biaxial bending.

Table 4. Four line vs. biaxial critical crack length analysis.

	VAS1 4 line	VAS1 biaxial	VAS2 4 line	VAS2 biaxial
Calculated mode I a_c [μm]	7.8–12.8	5.3–8.7	5.6–9.2	3.9–6.3
Measured largest crack length [μm]	10.3	5.6	7.8	5.3
Calculated edge/center length ratio	1.47		1.28	
Measured edge/center length ratio	1.84		1.47	

Assuming that the cracks leading to wafer fracture are half-circular surface cracks, LEFM gives the mode I stress intensity factor as[18]:

$$K_I = 1.1942\sigma\sqrt{\pi a} \quad (20)$$

Assuming mode I fracture toughness values from 0.86 to 1.1 MPa $\sqrt{m}$, the fracture strengths for the two testing approaches and the corresponding mode I fracture critical crack lengths are compared in Table 4. The largest measured crack length is also listed for comparison.

It can be seen that the calculated mode I critical crack length agrees well with the largest measured value. In addition, the table shows that the calculated and measured ratios of the mode I critical crack length for edge cracks to center cracks are also in reasonable agreement.

3. Conclusions

This paper compared the mechanical strengths of loose abrasive slurry and diamond wire sawn multicrystalline silicon PV wafers. Mechanical strength was evaluated as a function of microcrack location, size, orientation, and the strength measurement technique (four line bending versus biaxial flexure). Microcrack measurements showed that edge cracks are longer than center cracks for wafers produced under the same conditions. Diamond cut wafers were found to have a higher crack density while their expected crack length was smaller than for slurry cut wafers. It was also shown that cracks are longer in wafers cut by larger grits in slurry sawing (VAS1 vs. VAS2).

Through LEFM analysis, it was shown that in addition to crack length the crack orientation plays an important role in crack propagation due to the mixed mode fracture conditions present in the strength testing methods used. In four line bending, only cracks oriented at a small angle to the applied tensile stress can cause fracture. In contrast, crack orientation does not have a significant effect on the critical crack length in biaxial flexure tests.

The fracture strength obtained in four line bending tests was found to be directly correlated to wafer edge cracks while the biaxial test results were influenced by cracks in the wafer center. Due to the larger geometric factor in stress intensity calculations and longer cracks in the wafer edge, the four line

bending fracture strength was lower than the biaxial strength obtained for wafers cut under the same conditions.

The four line bending tests also revealed that diamond cut wafers have fracture strengths that are comparable to or superior to slurry cut wafers examined in this study. Consequently, from the standpoint of mechanical strength, the fixed abrasive diamond sawing technique can be an effective substitute for slurry wire sawing.

Acknowledgements: The authors are grateful to the financial support of the Silicon Solar Consortium (SiSoC), a National Science Foundation (NSF)—Industry/University Cooperative Research Center (I/UCRC). The authors would like to thank M. Seacrist of MEMC Electronic Materials and J. Cariaga of REC Wafers for providing the samples used in the tests.

Received: XXX[Q1]
Final Version: XXX

[1] H. J. Möller, C. Funke, M. Rinio, S. Scholz, *Thin Solid Films* **2005**, *487*, 179.
[2] R. F. Cook, *J. Mater. Sci.* **2006**, *41*, 841.
[3] P. A. Wang, *Proc. 4th WCPEC, Waikoloa, HI, USA*, **2006**, p. 1179.
[4] H. J. Möller, *Phys. Status Solidi A* **2006**, *203*(4), 659.
[5] F. Yang, I. Kao, *ASME J. Electron. Packag.* **2001**, *123*, 254.
[6] K. Bidiville, J. Wasmer, P. Michler, M. Nasch, M. Van der Meer, C. Ballif, *Prog. Photovolt.: Res. Appl.* **2010**, *18*, 563.
[7] Y. Kondo, N. Watanabe, D. Ide, T. Matsuki, H. Takato, I. Sakata, *Proc. 23rd EUPVSEC, Valencia, Spain*, **2008**, p. 1297.
[8] N. Watanabe, Y. Kondo, D. Ide, T. Matsuki, H. Takato, I. Sakata, *Prog. Photovolt.: Res. Appl.* **2010**, *18*, 485.
[9] A. Bidiville, K. Wasmer, R. Kraft, C. Ballif, *Proc. 24th EUPVSEC, 2CV.1, Hamburg, Germany*, **2009**, p. 86.
[10] X. Brun, S. Melkote, *Sol. Energy Mater. Sol. Cells* **2009**, *93*, 1238.
[11] P. Rupnowski, B. Sopori, *Int. J. Fracture* **2009**, *155*, 67.
[12] H. Behnken, M. Apel, D. Franke, *Proc. 3rd WCPEC, Osaka, Japan*, **2003**, p. 1308.
[13] A. Hayter, *Probability and Statistics for Engineers and Scientists*, Duxbury, California **2002**.
[14] B. Yeung, T. Y. Lee, *IEEE Trans. Compon. Packag. Technol.* **2003**, *26*(2), 423.
[15] T. L. Anderson, *Fracture Mechanics: Fundamentals and Applications*, Talyor & Francis Group, Florida **2005**.
[16] W. A. Weibull, *A statistical Theory of Strength of Materials*, Royal Swedish Institute for Engineering Research, Stockholm, Sweden **1959**.
[17] Standard practice for reporting uniaxial strength data and estimating Weibull distribution parameters for advanced ceramics, C1239-07. ASTM, Philadelphia, PA, USA, 2007.
[18] H. Tada, P. C. Paris, G. R. Irwin, (Eds), *The Stress Analysis Handbook*, ASME Press, New York **2000**.
[19] C. P. Chen, M. H. Leipold, *Am. Ceram. Soc. Bull.* **1980**, *59*, 469.
[20] J. Bagdahn, J. Schischka, M. Petzold, W. N. Sharpe, *Proc. SPIE* **2004**, *5581*, 159.
[21] I. Chasiotis, S. W. Cho, K. Jonnalagadda, *ASME J. Appl. Mech.* **2006**, *73*, 714.
[22] Tentative test method for biaxial flexure strength (modulus of rupture) of ceramic substrates, F394-74T. ASTM, Philadelphia, PA, USA, 1974.
[23] C. Funke, E. Kullig, M. Kuna, H. J. Möller, *Adv. Eng. Mater.* **2004**, *6*(7), 594.
[24] K. Mcguire, S. Danyluk, T. L. Baker, J. W. Rupnow, D. Mclaughin, *J. Mater. Sci.* **1997**, *32*, 1017.

Q1: Author: Please provide the history dates.

Q2: Author: Please check the suitability of the suggested short title.

*: Author: Please note that Figure for TOC will be printed in color.

Effect of Crystallographic Orientation on Ductile Scribing of Crystalline Silicon: Role of Phase Transformation and Slip

Hao Wu and Shreyes N. Melkote
The George W. Woodruff School of Mechanical Engineering
Georgia Institute of Technology
Atlanta, GA 30332

Abstract

This paper investigates the effect of crystallographic orientation on the mode of material removal (ductile vs. brittle) in diamond scribing of single crystal silicon (c-Si) and offers an explanation for the observed effects in terms of the combined role of phase transformation and slip generation. Single-point diamond scribing tests are performed on (111), (001) and (110) crystallographic planes in the <111>, <110>, <100> and <112> directions. In all cases, the material removal mechanism transitions from ductile to brittle fracture as the depth of scribing increases. The critical depth of ductile-to-brittle transition is found to vary considerably. Scribing on the (001) Si surface exhibits significant brittle fracture, while ductile removal is achieved on the (111) plane at scribing depths greater than 1μm. In addition, on a given crystallographic plane, brittle fracture is found to always dominate in the <100> direction compared to the <111> direction. These results are explained by the roles of phase transformation and slip generation in the material. For a given scribing depth, orientations for which slip systems are easily activated require higher loading pressures and therefore produce higher tensile stress in the material, which leads to increased brittle fracture. This explanation is found to be consistent with the experimental data presented in this paper and those available in literature.

Keywords: Silicon; Scribing; Ductile-to-brittle transition; Phase transformation; Slip

1. Introduction

Single crystal silicon (c-Si) is a brittle material at room temperature but is known to exhibit ductile mode deformation during machining/scribing [1-6]. Ductile mode cutting of c-Si is known to occur when the tool feed rate is less than a critical value determined by the material property [1]. Experiments have shown that ductile cutting of c-Si can be achieved by suitably controlling the tool tip radius and/or the undeformed chip thickness [5-6]. Analysis of stresses produced in silicon during cutting has shown that ductile removal is a result of the large compressive stress state immediately in front of the cutting tool, which suppresses the growth of pre-existing structural flaws in the material [7-8].

Given that mono c-Si is anisotropic, the effects of crystallographic orientation on ductile cutting have been studied by others [9-13]. Shibata et al. [9] reported the results of diamond turning experiments carried out on (111) and (001) crystal planes at cutting depths of 100 nm and 1μm. A slip orientation factor was proposed to explain the varying degrees of ductile mode cutting observed in different crystallographic orientations. However, this factor alone cannot explain the observations when scribing at a cutting depth of 1 μm. Moreover, their

explanation does not take into account the phase transformation of c-Si, which is believed to enable ductile mode cutting [14]. Similar observations were also reported in [10-13] when machining (turning) (111) and (001) c-Si, however no detailed scientific explanations for the observations were given.

In this paper, diamond scribing tests are carried out on the (111), (001) and (110) planes of c-Si in the <111>, <110>, <100> and <112> directions to investigate the effects of crystallographic orientation on the mode of material removal. In particular, the paper attempts to explain the observed differences in the modes of material removal in the different crystallographic planes/directions via arguments based on the effects of phase transformation and slip generation in c-Si during scribing.

2. Experiments

A single crystal cone shaped diamond scriber with 90° included angle was used in the scribing experiments reported here (Fig. 1). The tip radius was measured to be ~8μm. In the experimental setup, a semiconductor grade Czochralski (CZ) c-Si wafer was mounted on stacked X-Y-Z motion stages (Aerotech ANT-4V) and a Kistler 9257B 3-component piezoelectric cutting force dynamometer was used to measure the dynamic scribing forces (Fig. 2). The X-Y-Z stages have a positioning resolution of 1nm in the Z direction, thus permitting sub-micron depth scribing experiments. The scribing depth in the tests was increased linearly from 0- 2μm in order to study the ductile to brittle cutting mode transition. In addition, three scribing speeds of 1, 5 and 10 mm/min per crystal plane-orientation combination were used.

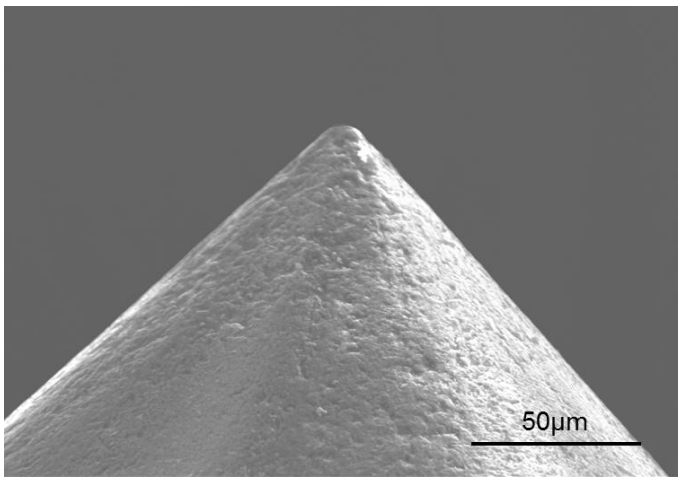

Figure 1. SEM image of diamond scriber used in the tests.

In the experiments, (111), (001) and (110) c-Si wafers were used. The orientations along which scribing was carried out are summarized in Table 1. Note that there is no data in the literature on the mode of material removal in diamond scribing of a (110) c-Si wafer.

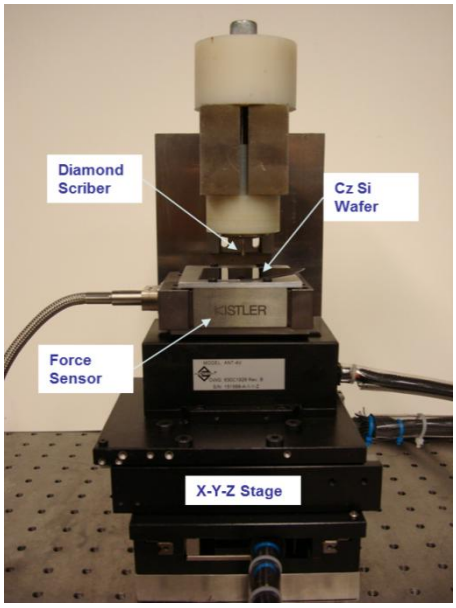

Figure 2. Scribing test setup.

Table 1. Scribing directions and critical depth as a function of scribing speed (V).

Plane	Scribing Direction	d_c (μm)			
		V1 (1mm/min)	V2 (1mm/min)	V3 (1mm/min)	Average
(111)	$[\bar{1}10]$	1.039	0.822	0.884	0.915
	$[\bar{1}\bar{1}2]$	0.341	0.314	0.519	0.391
(001)	[010]	0.100	0.145	0.122	0.122
	[110]	0.169	0.190	0.152	0.170
(110)	$[\bar{1}10]$	0.692	0.871	0.798	0.787
	[001]	0.234	0.201	0.220	0.218
	$[1\bar{1}\bar{1}]$	1.206	1.237	1.368	1.270

3. Results

The mode of material removal in all scribing tests was observed to change with cutting depth from completely ductile, to a combination of ductile and brittle, to completely brittle fracture. Representative Scanning Electron Microscope (SEM) images of the scribing tracks generated in the $(111)[\bar{1}\bar{1}2]$ orientation shown in Fig. 3 clearly reveal this trend. When the depth of scribing is small, ductile mode deformation is observed and the scribing track is very smooth and has no cracks. With increasing depth, surface cracks are observed at the edges of

the track while evidence of plastic flow can still be observed within the track. As the depth is increased further, significant evidence of brittle fracture is observed with little or no evidence of ductile cutting.

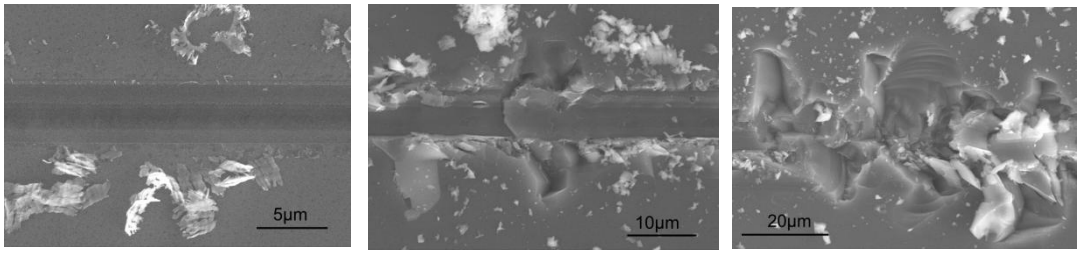

Figure 3. Surface morphology of diamond scribed track in (111)$[\bar{1}\bar{1}2]$ c-Si at 1mm/min scribing speed and scribing depths of 0.123 μm (left), 0.722 μm (middle), and 1.225 μm (right), scribing direction is left to right.

While the general surface morphology trends are similar in all the tests, certain crystallographic orientations exhibit greater ductile mode behavior than others. Similar to previous work [3-8], a critical depth of scribing d_c is used here to quantitatively compare the different test cases. The critical depth is defined here as the depth at the location along the track where brittle fracture is first observed. A large value of d_c implies good ductile machinability of the material. The critical depth is measured by means of a confocal microscope (LEXT 3D). Figure 4 shows a sample image and the procedure used to determine the critical depth.

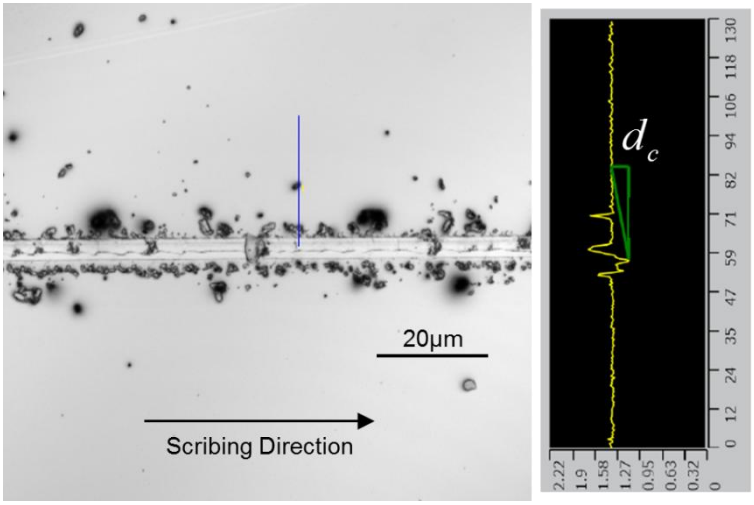

Figure 4. Measurement of critical depth of scribing d_c.

The critical depths obtained in the scribing tests are summarized in Table 1. It can be seen that the critical depths in the (001) plane are much smaller than in the other crystal planes, which implies significantly reduced ductile cutting. For tests in the same plane, scribing in the <111> direction exhibits greater ductile behavior than in the <110> direction, while brittle fracture is dominant in the <100> direction. For the range of scribing speeds tested, the effect of scribing speed on the critical depth does not appear to be significant.

Figure 5 summarizes other interesting surface features seen in the SEM images. Parallel chevron cracks, are observed along the edges of the (111)$[\bar{1}10]$ track and tend to propagate in the (111)$[01\bar{1}]$ direction. Severe cracking is observed immediately following pure ductile mode cutting when scribing the (001) wafer. Large pits due to cracking are clearly visible in the (001) [010] track even at small depths of cut. In contrast, complete ductile mode cutting is observed in the (110)$[1\bar{1}\bar{1}]$ track even at scribing depths greater than 1 μm. Note that scribing in the <111> orientation is only possible in the (110) wafer.

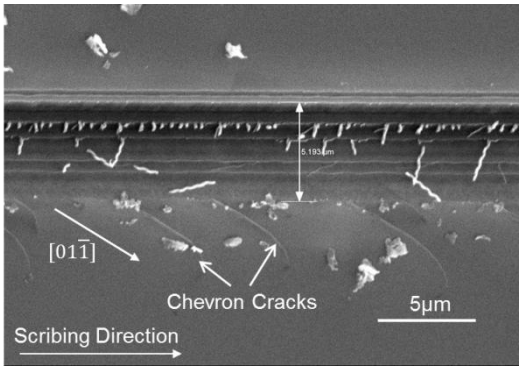

(111)$[\bar{1}10]$ track, 1mm/min

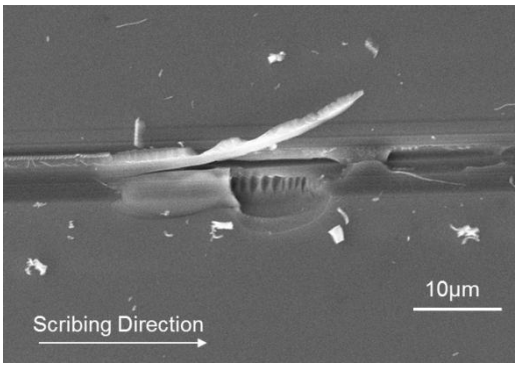

(001)[110] track, 1mm/min

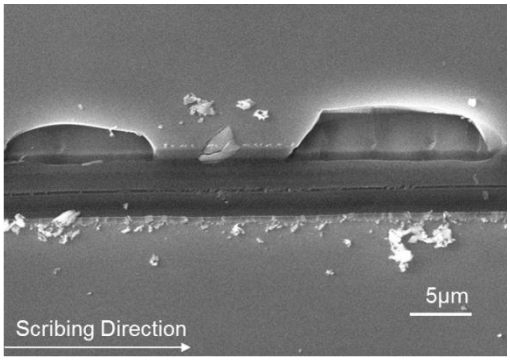

(001)[010] track, 1 mm/min

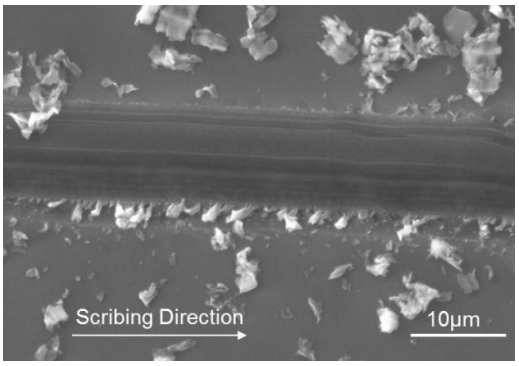

(110)$[1\bar{1}\bar{1}]$ track, 1 mm/min

Figure 5. Morphology of the scribing tracks.

4 Discussion

4.1 *Phase transformation of Si during scribing*

It is well-established that even though c-Si retains its diamond cubic structure at atmospheric pressure, it can be transformed into other phases (crystalline and amorphous) at higher pressures. For instance, at pressures of 10-12 GPa [15], Si-I transforms into a denser BCT β-Sn phase (Si-II), accompanied by a 22% volumetric reduction. Further increases in hydrostatic pressure can result in other phases (Si-V, Si-VI, Si-VII, etc). Upon unloading, the high pressure phases transform back to Si-II [16]. With further unloading Si-XII (metastable rhombohedra structure) and Si-III (body centered cubic) can form, with amorphous silicon (a-Si) forming when the unloading rate is above a critical value and does not provide sufficient time for recrystallization [17-22]. Note that Si-III, Si-XII and amorphous silicon

phases are observed mostly in areas where ductile cutting is observed [17]. Raman spectra from the ductile portion of the track show no evidence of the diamond cubic phase of c-Si, and in most cases reveal only a-Si. It is interesting to note that Si-XII and Si-III metastable phases were observed only in the test conducted at the low speed of 1 mm/min in the (110) [001] direction. The low scribing speed corresponds to a low unloading rate, which likely leads to the formation of the crystalline phases. Representative Raman spectra of the scribed track are shown in Fig. 6. It can be seen that the broad peaks at 480 and 170 cm^{-1} correspond to a-Si [23]. Figure 7 shows peaks at Raman shifts of 430 and 350 cm^{-1}, which indicate the presence of Si-XII and Si-III phases, respectively [18].

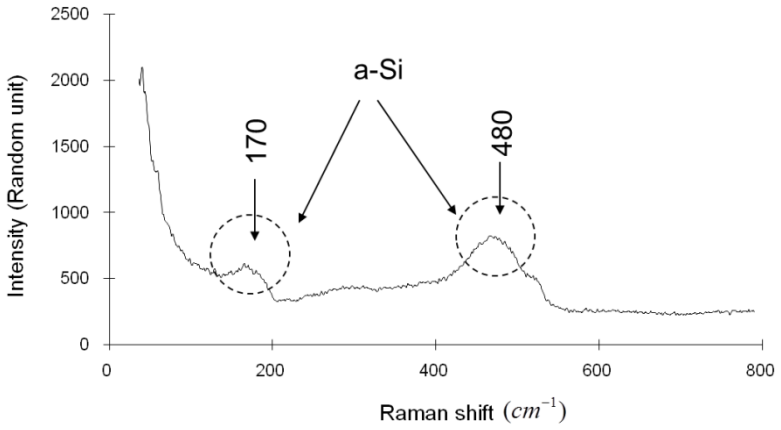

Figure 6. Raman spectra of (110) [001] track at 5 mm/min scribing speed.

In regions where both cracking and ductile flow are observed, both diamond cubic and a-Si phases are present, whereas only the diamond cubic Si phase is present in areas of brittle fracture. This confirms that the ductile flow behavior observed in the scribing tests is caused by the phase transformation of c-Si.

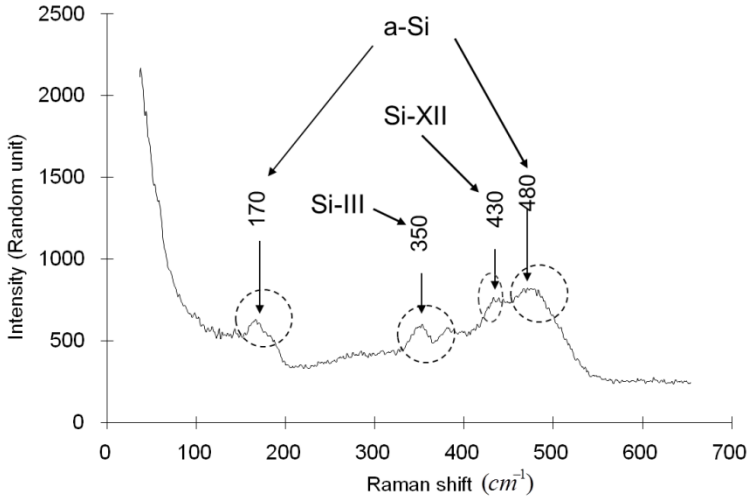

Figure 7. Raman spectra of (110) [001] track scribed at 1mm/min.

4.2 *Dislocation generation in scribing of silicon*

Prior studies in c-Si suggest that there is no dislocation generation in conventional mechanical testing at temperatures below 450° [24]. However, evidence of slip due to dislocation motion in silicon has been widely observed under extreme loading conditions such as in indentation and scribing [25-29] where localized stresses can approach the theoretical shear strength of silicon. In fact, evidence of slip through dislocation motion has been shown in micro-indentation tests under all loading conditions, irrespective of whether the maximum load exceeds the required load for phase transformation or not [29]. The high localized hydrostatic stress directly underneath a sharp indenter is believed to be the cause of phase transformation, while the shear stress on the {111} slip planes of c-Si are believed to provide the driving force for slip [25-26]. It has been shown in previous studies that dislocations travel in the {111} plane after nucleation until their progress is halted by intersection with other dislocations or by intersection with the free surface. This produces the characteristic "V" shape of the dislocation slip bands reported in literature (see Fig. 8). Moreover, when indenting c-Si, the sequence of deformation consists of initial deformation via slip followed by phase transformation when the critical pressure for transformation is reached [27].

The hydrostatic and shear stresses generated in scribing can be as high as in indentation, and therefore a similar material response under load, i.e. slip generation and phase transformation, is to be expected. In fact, cross-sectional TEM images of diamond turned silicon show evidence of dislocations in the {111} plane and <110> direction, as well as a-Si layer on the surface [29].

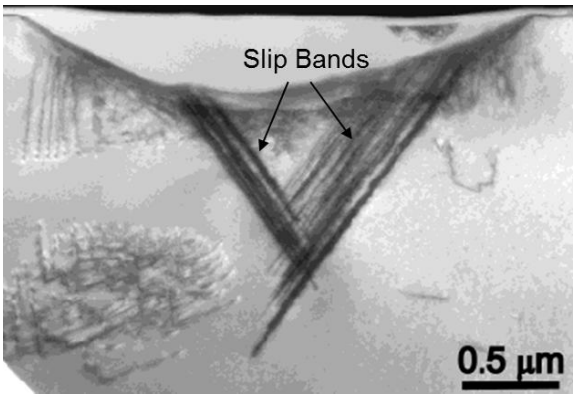

Figure 8. TEM image of indentation in c-Si made using a spherical indenter (after Bradby et al. [28]); clear evidence of slip bands can be seen.

While the experimental evidence in this work confirms the role of phase transformation in ductile mode scribing, the reason for the orientation dependence of the scribing mode is not that obvious and requires further scrutiny. It is hypothesized that this dependence of the mode of cutting on crystallographic orientation is due to differences in the ease of activating slip systems in c-Si. The Schmid factor is commonly used to evaluate the likelihood of activating slip systems in a particular orientation of the crystal and is given by $\cos\varphi \times \cos\lambda$, where φ is the angle between the loading direction and the direction normal to the slip plane,

and λ is the angle between the loading and slip directions. A large Schmid factor indicates a large magnitude of the resolved shear stress under the same load and therefore a higher likelihood for slip generation in that direction. Table 2 lists the Schmid factors for all twelve {111} <110> possible slip systems in diamond cubic silicon for the loading directions used in the current work. Note that there are two major loading directions in the scribing tests reported here, one normal to the wafer surface and the other along the scribing direction. The third scribing force component, which is perpendicular to both the normal and scribing directions, is negligible.

It can be seen that loading in <111> yields small Schmid factors, which implies that only six slip systems are likely to be activated, while loads in the <100> direction have the largest Schmid factors leading to the activation of eight of the twelve slip systems. The Schmid factors are also large along <110> but will activate only four of the twelve slip systems. The scribing tests with larger Schmid factors will activate more slip systems and will therefore induce more slip. For instance, scribing in the {111} <110> direction, where the normal load is in the <111> direction and the tangential load is in the <110> direction, tends to generate fewer dislocations than scribing in the {100} <100> orientation, where both normal and tangential loading directions belong to the <100> family of directions, because of smaller Schmid factors and fewer activated slip systems (non-zero Schmid factor) in <111> and <110> directions than in <100> .

Table 2. Schmid factors of loading orientations tested in the experiment.

Slip Plane	Burgers Vector Orientation	Schmid Factor			
		[$\bar{1}\bar{1}$2] (<112>)	**[$\bar{1}$10] (<110>)**	**[010] (<100>)**	**[1$\bar{1}\bar{1}$] (<111>)**
($1\bar{1}\bar{1}$)	**[$\bar{1}$0$\bar{1}$]**	0.2722	0.4082	0	0
	[0$\bar{1}\bar{1}$]	0.2722	0.4082	0.4082	0.2722
	[$\bar{1}$10]	0	0	0.4082	0.2722
($1\bar{1}$1)	**[0$\bar{1}\bar{1}$]**	0.1361	0	0.4082	0.2722
	[10$\bar{1}$]	0.4082	0	0	0.2722
	[110]	0.2722	0	0.4082	0
($\bar{1}$11)	**[$\bar{1}$0$\bar{1}$]**	0.1361	0	0	0
	[01$\bar{1}$]	0.4082	0	0.4082	0
	[110]	0.2722	0	0.4082	0
(111)	**[01$\bar{1}$]**	0	0.4082	0.4082	0
	[10$\bar{1}$]	0	0.4082	0	0.2722
	[$\bar{1}$10]	0	0	0.4082	0.2722

It is well known that the indentation hardness of a crystalline material exhibiting ductile behavior is a function of dislocation density [30]. Basically, indentation hardness is higher for a material with higher dislocation density. This implies that a higher load (or pressure) is required to induce the same depth of indentation in a material with higher dislocation density.

Therefore, larger applied load (or pressure) is required to cause the same depth of indentation/scribing along crystallographic directions that are characterized by larger Schmid factors. For a given scribing depth, scribing along <100> requires higher pressure and therefore generates a larger stress in the material than scribing in the <110> or <111> orientations. While the compressive stress caused by the applied load (or pressure) may cause phase transformation, the corresponding tensile stress generated in the material will cause fracture if the stress intensity factor exceeds the material's fracture toughness. For the three possible modes of crack propagation, namely the crack opening mode (mode I), the in-plane shear mode (mode II), and the out-of-plane shear mode (mode III), the stress intensity factors can be expressed as [31]:

$$K_{(I,II,III)} = Y\sigma\sqrt{\pi a} \tag{5}$$

where σ is the applied stress, a is the characteristic crack dimension and Y is a dimensionless constant that depends on the geometry and the loading mode. As the applied stress σ increases, the value of K also increases and when K exceeds the fracture toughness (K_c) of the material, the crack propagates and fracture occurs. In scribing tests along different orientations but the same scribing depth, the orientation requiring a larger pressure will more easily cause the stress intensity factor to exceed the facture toughness and therefore will exhibit more fracture. Thus, the scribing test in <100> will exhibit greater fracture than in <110>, while scribing in the <111> direction will exhibit the least fracture (and therefore the greatest ductile flow).

The foregoing analysis is consistent with experimental observations summarized in Table 1. For example, when scribing in the (110) plane, the critical depth of scribing d_c is largest along $[1\bar{1}\bar{1}]$, and is somewhat smaller along $[\bar{1}10]$, and is least along [001]. For scribing tests in the same family of directions but in different crystallographic planes, differences in ductile cutting are determined by the ease of dislocation generation in orientations normal to the planes. Taking the scribing tests along $(111)[\bar{1}10]$ and $(110)[\bar{1}10]$ for comparison, although both cases represent scribing along the <110> family of directions, loading at the same depth along <111> will induce less cracking than along <110>. Thus, scribing along $(111)[\bar{1}10]$ should produce more ductile behavior than along $(110)[\bar{1}10]$. This is confirmed by the higher experimentally observed value of d_c along $(111)[\bar{1}10]$.

Based on the foregoing analysis, it can be concluded that, for a given depth of cut, scribing along an orientation with a large Schmid factor will activate more slip systems, which in turn increases the material strength and therefore the tensile stress generated in the material, leading to increased brittle fracture. In contrast, orientations with fewer slip systems and smaller Schmid factors exhibit more ductile behavior.

5. Conclusion

Crystallographic orientation dependence of ductile mode scribing in c-Si is investigated via increasing depth diamond scribing experiments. It is found that scribing in the (111) plane exhibits more ductile cutting than in the (110) plane, while the greatest amount of brittle fracture is found when scribing in the (001) plane. For scribing in the same plane, the <111>

direction tends to exhibit much more ductile cutting than the <100> direction. Raman spectra-based phase analysis of the scribed tracks indicates that ductile mode behavior of c-Si is achieved through phase transformation from Si-I to Si-II during loading and, depending on the unloading rate, to a-Si or Si-XII and Si-III phases. It is concluded that loading in an orientation with the largest Schmid factor tends to activate more slip systems through generation and motion of dislocations, which trap each other and thereby strengthen the material. This strengthening in turn implies that a higher pressure is required for the same depth of scribing. The higher pressure produces a larger tensile stress, which results in increased brittle fracture.

6. Acknowledgement

The authors are grateful for the financial support of this work by the Silicon Solar Consortium (SiSoC), a National Science Foundation (NSF) - Industry/University Cooperative Research Center (I/UCRC). The authors would also like to thank M. Seacrist of MEMC Electronic Materials for providing the c-Si samples used in tests.

7. References

1. T. G. Bifano, T. A. Dow, and R. O. Scattergood, "Ductile-regime grinding: a new technology for machining brittle materials," ***Trans. ASME, J. Engng for Industry***, 1991. **113**(2): p. 184-189.
2. C. G. Scott and S. Danyluk, "Examination of silicon wear debris generated in a linear scratch test," ***Wear***, 1992. **152**: p. 183-185.
3. M. Zhou, et al., "Brittle-ductile transition in diamond cutting of silicon single crystal," ***Materials and Manufacturing Processes***, 2001. **16**(4): p. 447-460.
4. F. Z. Fang and G. X. Zhang, "An experimental study of edge radius effect on cutting single crystal silicon," ***Int J Adv Manuf Technol***, 2003. **22**: p. 703-707.
5. X. P. Li, et al., "Study of the upper bound of tool edge radius in nanoscale ductile mode cutting of silicon wafer," ***Int J Adv Manuf Technol***, 2010. **48**(993-999).
6. K. Liu, et al., "A study of the effect of tool cutting edge radius on ductile cutting of silicon wafers," ***Int J Adv Manuf Technol***, 2007. **32**: p. 631-637.
7. K. Liu, X. P. Li, and S. Liang, "The mechanism of ductile chip formation in cutting of brittle material," ***Int J Adv Manuf Technol***, 2007. **33**: p. 875-884.
8. M. B. Cai, X. P. Li, and M. Rahman, "High-pressure phase transformation as the mechanism of ductile chip formation in nanoscale cutting of silicon wafer," ***Proc. IMechE, Part B: J. Engineering Manufacture***, 2007. **221**(10): p. 1511-1519.
9. T. Shibata, et al., "Ductile-regime turning mechanism of single-crystal silicon," ***Precision Engineering***, 1996. **18**: p. 129-137.
10. N. P. Hung and Y. Q. Fu, "Effect of crystalline orientation in the ductile-regime machining of silicon," ***Int J Adv Manuf Technol***, 2000. **16**: p. 871-876.
11. J. Yan, et al., "Ductile regime turning at large tool feed," ***J.Mater.Process.Tech***, 2002. **121**: p. 363-372.
12. C. Chao, et al., "Ductile behaviour in single-point diamond-turning of single-crystal silicon," ***J.Mater.Process.Tech***, 2002. **127**: p. 187-190.

13. B. O'Connor, E. Marsh, and J. Couey, "On the effect of crystallographic orientation on ductile material removal in silicon," ***Precision Engineering***, 2005. **29**: p. 124-132.
14. J. C. Morris and D. L. Callahan, "Origins of microplasticity in low-load scratching of silicon," ***J. Mater.Reser***, 1994. **9**(11): p. 2907- 2913.
15. J. Hu, et al., "Crystal data for high-pressure phases of silicon," ***Phys. Rev. B***, 1986. **34**(7): p. 4679-4684.
16. S. Duclos, Y. Vohra, and A. Ruoff, "Experimental study of the crystal stability and equation of state of Si to 248 GPa," ***Phys. Rev. B***, 1990. **41**(17): p. 12021-12028.
17. Y. Gogotsi, et al., "Raman microspectroscopy analysis of pressure-induced metallization in scratching of silicon," ***Semicond. Sci. Technol***, 2001. **16**(5): p. 345-352.
18. A. Kailer, Y. Gogotsi, and K. Nickel, "Phase transformations of silicon caused by contact loading," ***J.Appl.Phys***, 1997. **81**(7): p. 3057-3063.
19. S. Ruffell, et al., "High pressure crystalline phase formation during nanoindentation: amorphous versus crystalline silicon," ***Appl. Phys. Lett***, 2006. **89**: 091919.
20. B. Haberl, et al., "Phase transformations induced in relaxed amorphous silicon by indentation at room temperature," ***Appl. Phys. Lett***, 2004. **85**(23): p. 5559-5561.
21. I. Zarudi, et al., "Microstructure evolution in monocrystalline silicon in cyclic microindentations," ***J. Mater. Res***, 2003. **18**(4): p.758-761.
22. I. Zarudi, et al., "The Ra-BC8 phases and crystal growth in monocrystalline silicon under microindentation with a spherical indenter," ***J. Mater. Res,*** 2004. **19**(1): p.332-337.
23. J. Smith, et al., "Raman spectra of mmorphous Si and related tetrahedrally bonded semiconductors," ***Phys.Rev.Lett***, 1971. **26**(11): p. 642-646.
24. H. Alexander and P. Haasen, "Dislocations and plastic flow in the diamond structure," ***Solid State Phys***, 1968. **22**: p. 27.
25. I. Zarudi, J. Zou, and L.C. Zhang, "Microstructures of phases in indented silicon: A high resolution charaterization," ***Appl. Phys. Lett***, 2003. **82**(6): p. 874-876.
26. H. Sakaa, et al., "Transmission electron microscopy of amorphization and phase transformation beneath indents in Si," ***Philos. Mag. A***, 2002. **82**(10): p. 1971-1981.
27. J. E. Bradby, et al., "Transmission electron microscopy observation of deformation microstructure under spherical indentation in silicon," ***Appl. Phys. Lett***, 2000. **77**(23): p. 3749-3751.
28. J. E. Bradby, J. Williams, and J. Wong-Leung, "Mechanical deformation in silicon by micro-indentation," ***J.Mater.Res.***, 2001. **16**(5): p. 1500-1507.
29. T. Shibata, et al., "Cross-section transmission electron microscope observations of diamond-turned single-crystal Si surfaces," ***Appl. Phys. Lett***, 1994. **65**(20): p. 2553-2555.
30. W. Nix and H. Gao, "Indentation size effects in crystalline materials: a law for strain gradient plasticity," ***J.Mech.Phys.Solids***, 1998. **46**(3): p. 411-425.
31. T.L.Anderson, ***Fracture Mechanics: Fundamentals and Applications***. 3rd ed. 2005, Florida: Talyor & Francis Group.

Appendix A-4: under review, ASME J. Engineering Materials & Technology; Abbreviated version in Proc. of 26th European Photovoltaic Solar Energy Conference and Exhibition, pp. 966-970.

MODELING AND ANALYSIS OF DUCTILE-TO-BRITTLE TRANSITION IN DIAMOND SCRIBING OF SILICON: APPLICATION TO WIRE SAWING OF SILICON WAFERS

Hao Wu and Shreyes N. Melkote
The George W. Woodruff School of Mechanical Engineering
Georgia Institute of Technology
Atlanta, GA, USA 30332

ABSTRACT

The ductile-to-brittle cutting mode transition in single grit diamond scribing of monocrystalline silicon is investigated in this paper. Specifically, the effects of scriber tip geometry, coefficient of friction and external hydrostatic pressure on the critical depth of cut associated with ductile-to-brittle transition and crack generation are studied via an eXtended Finite Element Method (XFEM) based model, which is experimentally validated. Scribers with a large tip radius are shown to produce lower tensile stresses and a larger critical depth of cut compared to scribers with a sharp tip. Spherical tipped scribers are shown to generate only surface cracks while sharp tipped scribers (conical, Berkovich and Vickers) are found to create large subsurface tensile stresses, which can lead to nucleation of subsurface median/lateral cracks. Lowering the friction coefficient tends to increase the critical depth of cut and hence the extent of ductile mode cutting. The results also show that larger critical depth of cut can be obtained under external hydrostatic pressure. This knowledge is expected to be useful in optimizing the design and application of the diamond coated wire employed in fixed abrasive diamond wire sawing of photovoltaic silicon wafers.

Keywords: Diamond scribing, silicon, modeling, ductile-to-brittle transition, crack, scriber shape, wire sawing

1 INTRODUCTION

While loose abrasive slurry sawing is the dominant process for producing photovoltaic (PV) silicon wafers [1-2], fixed abrasive diamond wire sawing is rapidly gaining attention due to its potential for higher productivity [3-4]. In order to understand the basic cutting mechanisms involved in the diamond wire sawing process and their effect on surface integrity of silicon wafers, a fundamental study of the mechanics of interaction between a single abrasive grit (or scriber) and silicon is necessary and forms the focus of this paper.

Although silicon is brittle at room temperature, it exhibits ductile behavior when cut at low feed rates [5]. A number of studies focused on ductile mode cutting of crystalline silicon have been reported [6-15]. It is widely believed that ductile behavior of silicon is due to transformation of the diamond cubic phase of silicon to a metallic phase under high contact pressures [9-15].

Figure 1 shows the typical cutting mode transition with increasing cutting depth in single grit diamond scribing experiments on monocrystalline silicon performed under ambient conditions. It can be seen that as the scribing depth increases, there is transition from purely ductile mode cutting, which yields a smooth crack-free surface, to a mix of ductile and brittle fracture and then to complete brittle fracture.

Prior work has shown that the critical depth for transition from ductile to brittle mode of cutting is given by [5]:

$$d_c = 0.15 \left(\frac{E}{H}\right)\left(\frac{K_c}{H}\right)^2 \tag{1}$$

where K_c is the fracture toughness, H is the hardness and E the elastic modulus. This expression, while useful, does not explicitly account for the effects of scriber tip geometry, friction, etc. Cutting experiments on silicon indicate that the critical depth varies with changing tip radius [7-9].

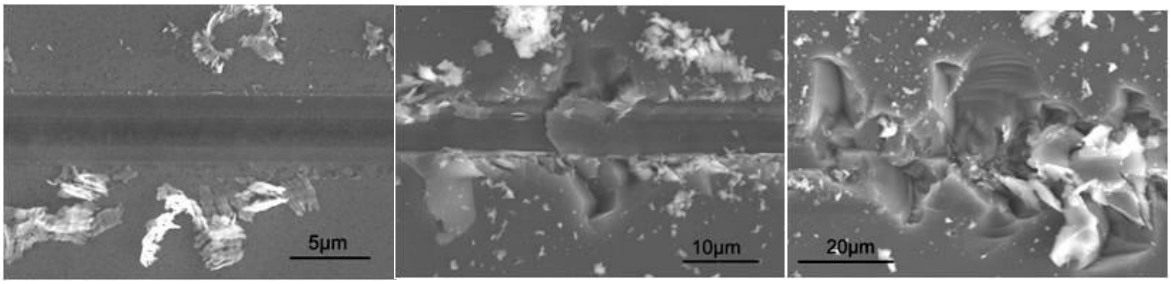

Figure 1. Surface morphology in diamond scribing of (111) mono silicon at depths of 0.123 μm (left), 0.722 μm (middle), and 1.225 μm (right); spherical tip scriber with 8 μm tip radius used.

Prior work on ductile cutting of silicon is limited to single point turning or scribing experiments with a diamond tool of a specific tip geometry [7-11]. In contrast, fixed abrasive diamond wire sawing is characterized by a wide distribution of grit shapes, sizes, tip radii and cutting conditions, whose effects are not well-understood. Consequently, this paper investigates the effects of diamond grit shape, coefficient of friction and cutting depth on the ductile-to-brittle transition in diamond scribing of monocrystalline silicon using the eXtended Finite Element Method (XFEM) to model crack initiation and propagation during the scribing process.

2 MODELING

2.1 XFEM overview

The XFEM is an extension of the conventional finite element method for structural analysis and allows modeling of 3D nucleation of discontinuities (e.g. cracks) in the material without requiring explicit remeshing of the crack surfaces [16-17]. A discontinuous jump function and asymptotic crack-tip displacement fields are added to the finite element approximation to account for the crack using the notion of partition of unity . The presence of discontinuity in the material is modeled via special enrichment functions in conjunction with

additional degrees of freedom. This is accomplished using the displacement vector function u as follows [18]:

$$u = \sum_{I=1}^{N} N_I(x)[u_I + H(x)a_I + \sum_{\alpha=1}^{4} F_\alpha(x)b_I^\alpha] \quad (2)$$

where $N_I(x)$ are the nodal shape functions; u_I is the nodal displacement vector for the continuous part of the finite element solution; the second term is the product of the nodal enriched degree of freedom vector, a_I, and the discontinuous jump function $H(x)$ across the crack surfaces; the third term is the product of the nodal enriched degree of freedom vector, b_I^α, and the elastic asymptotic crack-tip functions, $F_\alpha(x)$. Additional details of the XFEM approach can be found in [18]. The first term on the right-hand side of Eq. (2) is applicable to all the nodes in the model; the second term is valid for nodes of elements that are intersected by the crack; and the third term is used only for nodes of the element that contains the crack tip. In the present work, the XFEM formulation available in the commercial finite element code ABAQUS/Standard 6.10 is used to build the model.

Note that damage (crack) modeling is achieved via a traction-separation law and follows the general damage modeling framework in ABAQUS 6.10, including specification of a damage initiation criterion and damage evolution law, which are defined as material properties.

2.2 Material properties

In order to simulate the mechanical interaction of a diamond scriber with silicon using XFEM, a constitutive model for the material behavior must be defined. Under tensile load, silicon typically undergoes elastic deformation till fracture. However, it undergoes phase transformation when subjected to a sufficiently high hydrostatic stress [19]. Therefore, the

constitutive model must account for both phase transformation and elastic-fracture characteristics.

Under tensile load, the anisotropic elastic property of silicon is defined as:

$$\sigma_{ij} = C_{ijkl}\,\varepsilon_{kl} \quad \text{or} \quad \varepsilon_{ij} = S_{ijkl}\,\sigma_{kl} \tag{3}$$

where C is the stiffness matrix and S is the compliance matrix. Since it is of interest here to model the scribing process in (111) silicon in the <110> orientation, the elements of C and S can be identified through crystallographic transformation [20].

Since transformations from the Si-II phase to higher pressure phases are reversible [21], only the property of Si-II is included in the material model. The general behavior of silicon in compression is modeled as elastic-plastic. As shown in Fig. 2, silicon exhibits anisotropic elastic behavior below point 1, while it behaves plastically after point 1. The region between point 1 (corresponding to the lowest pressure for Si-I to Si-II transformation [22]) and point 2 (corresponding to the highest pressure for Si-I to Si-II transformation [19]) represents the region of phase transformation to Si-II. Between points 2 and 3 (where Si-II to Si-V transformation ocurrs [19]), Si-II is assumed to exhibit linear hardening behavior under uniaxial loading. The material constants for phase transformation are calculated from the transformation pressure data reported in literature and reproduced in Table 1.

The fracture strength of (111) silicon is used as the crack initiation criterion. Since there is a wide variation in fracture strength data reported in the literature, a fracture strength of 4 GPa derived from surface acoustic wave pulse tests on monocrystalline silicon without any pre-crack or notch [23] is used in this work. The crack propagation criterion is defined in terms of the energy release rate as follows:

$$G \geq G_c = 2w_f \tag{4}$$

where $G$is the energy release rate, $G_c$is the fracture toughness, w_f is the energy needed to create a new surface and is equal to 1.15 $\mathrm{J/m^2}$ for {111} cleavage plane [24].

Table 1. Material property constants used for phase transformation model

Point	Stress (GPa)	True Strain	Effective Plastic Strain
1	8.8 [22]	0.0518	0
2	11.2 [19]	0.4166	0.349
3	16.4 [19]	0.4578	0.3588

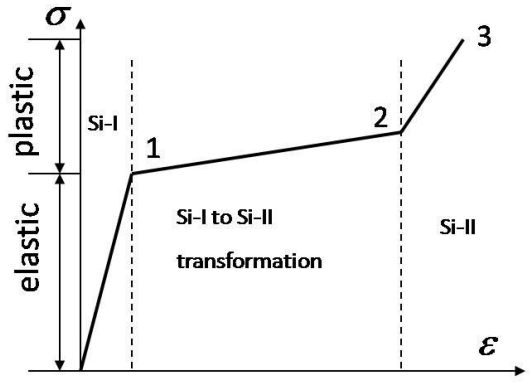

Figure 2. Constitutive material model for silicon.

2.3 Scriber geometry and process

Initially, only two scriber tip shapes are modeled and compared with experimental results. Scriber I has a truncated conical shaped tip of 60° included ange with a flat top of 10 μm diameter (see Fig. 3). Scriber II (see Fig.4) is conical with a 120° included angle and a tip radius of 3 μm. Frictional contact between the scriber surfaces and silicon is modeled and the friction coefficient is varied between 0.1 and 0.2. These values are estimated from force measurements made in scribing tests performed in air. Note that the coefficient of friction variation is intended to simulate variation in the cutting fluid properties used in the diamond wire sawing process.

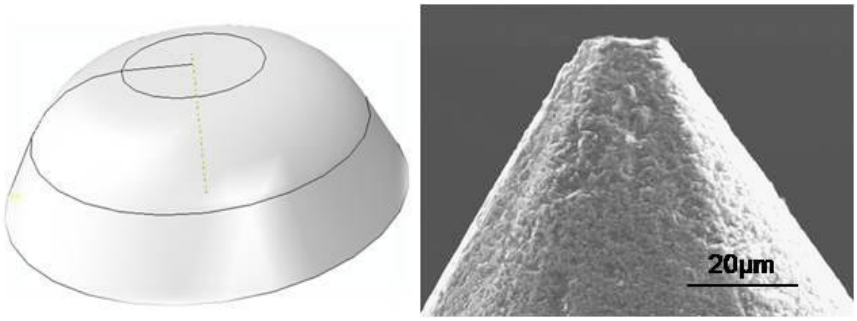

Figure 3. Scriber I geometry (sketch on left is model of scriber tip portion only).

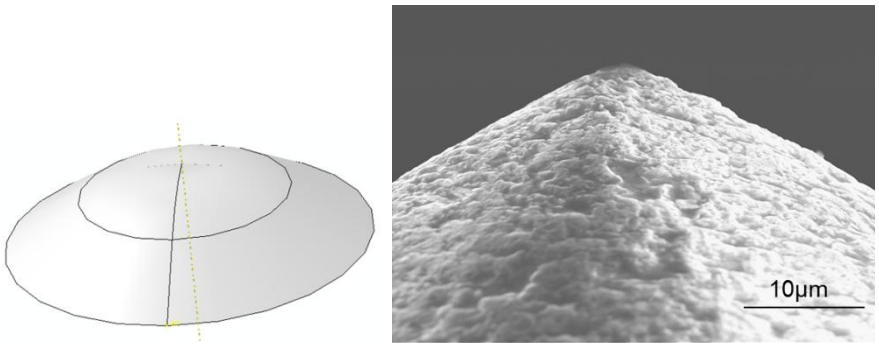

Figure 4. Scriber II geometry (sketch on left is model of scriber tip portion only).

A gradually increasing depth of cut is used to simulate the scribing process. Also, due to symmetry in the scribing geometry, only a one-half 3D model of the scribing process is built and solved. Note that preliminary simulations showed that no cracks nucleate in the plane of symmetry. Finally, it should be noted that the model does not consider removal of material during scribing.

3 RESULTS

3.1 Model simulations

The principal stress contours for the two scriber geometries have similar features and therefore only the results for Scriber II are shown in Fig. 5. It can be seen that as the scribing

depth increases, the compressive stress field directly under the scriber and the tensile stress field behind the scriber tip increase in magnitude. At a certain location along the scribing direction, the tensile stress exceeds the fracture strength criterion and surface cracks nucleate and propagate when the energy release rate exceeds the fracture toughness of the material. Note that the semi-circular crack path follows the tensile stress contours.

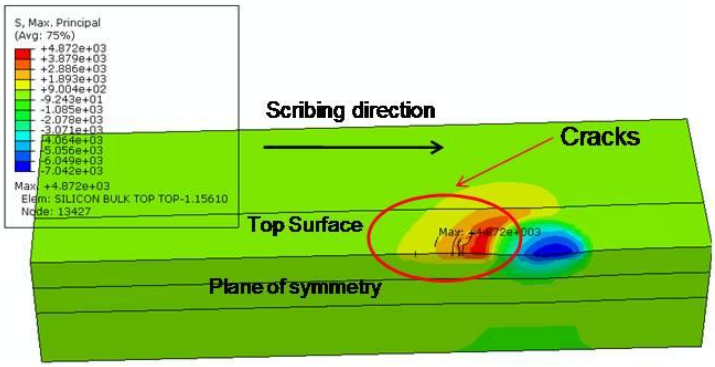

Figure 5. Principal stress and crack generation for Scriber II (scriber not shown).

As shown in Fig. 6, two types of semi-circular (or "chevron") cracks are observed in the two scribing simulations. Type I refers to crack propagation that starts from the center of the scribing track and curves outward in accordance with the large tensile stress region. Type 2 cracks are initiated from outside the scribing track and follow the maximum tensile stress region towards the center of the scribing track.

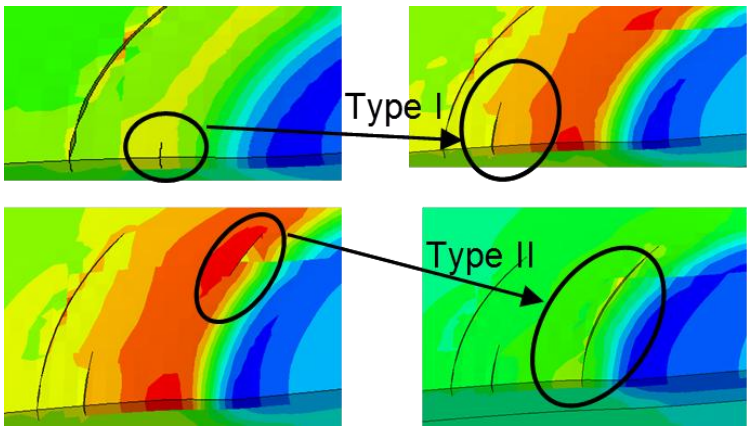

Figure 6. Crack propagation patterns (left figures: crack initiation, right figures: crack propagation).

Figure 7 shows the evolution of principal (tensile) stress with scribing depth for the two scriber shapes used in the simulations. It is seen that the tensile stress increases sharply with increase in cutting depth for Scriber II, while the increase is more gradual for Scriber I. Consequently, the critical depth of cut (which corresponds to the crack initiation point) is much greater for the blunt scriber (Scriber I) than for the sharp scriber (Scriber II). The hydrostatic pressures corresponding to the crack initiation points are 9.45 GPa and 9.19 GPa, respectively, which are sufficiently high for phase transformation of silicon. Consequently, ductile mode of cutting is expected prior to crack initiation.

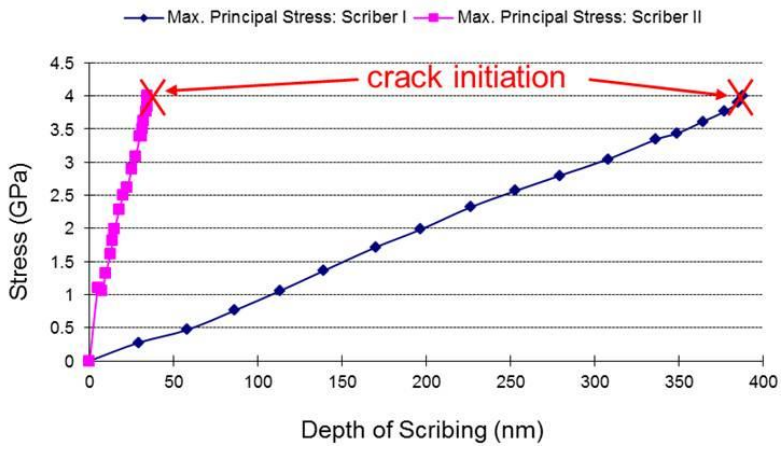

Figure 7. Evolution of stress with scribing depth.

3.2 Validation experiments

Gradually increasing depth of cut (0-2µm) single grit diamond scribing experiments were carried out on a polished CZ silicon wafer in the (111) <110> orientation to validate the XFEM model. A semiconductor grade Czochralski (CZ) c-Si wafer was mounted on stacked X-Y-Z motion stages (Aerotech ANT-4V) and a Kistler 9257B 3-component piezoelectric cutting force dynamometer was used to measure the dynamic scribing forces (see Fig. 8). The X-Y-Z stages have a positioning resolution of 1nm in the Z direction, thus permitting sub-micron depth scribing experiments. Note that all the tests were performed under ambient conditions without any cutting fluid. The two scriber geometries used in the model simulations discussed previously were employed in the actual tests.

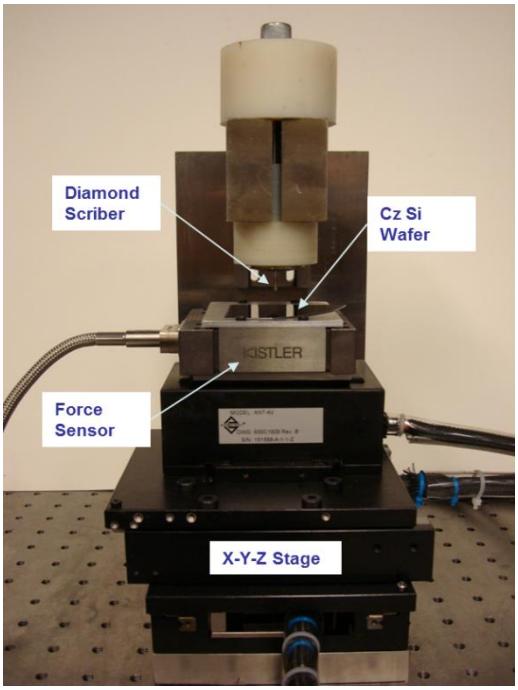

Figure 8. Scribing test setup

Figure 9 shows a comparison of the surface morphology (see SEM image) obtained with Scriber I and the corresponding model simulation result. It can be seen that the simulated and predicted crack paths are similar. Prior to crack initiation in the experiment, the track produced by the scriber clearly shows evidence of ductile cutting. The simulated critical depth of cut (387.6 nm) is in reasonable agreement with the measured depth (318±37.2 nm). For

Scriber II, the simulated critical depth (34.6 nm) was also found to be in reasonable agreement with the measured depth (52.1±7.7 nm). Differences in the measured and simulated critical depths can be attributed to the idealized model of the scriber geometry, variation in the fracture strength of silicon, and difficulty in precisely identifying the first crack initiation point in the experiment.

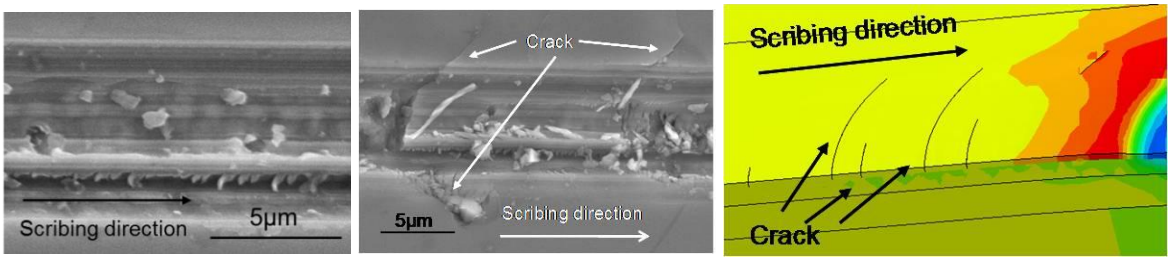

(a) (b) (c)

Figure 9. (a) Ductile flow prior to crack, (b) measured, and (c) simulated crack paths for Scriber I.

3.3 Effects of scriber shape and friction

The validated XFEM model was used to analyze the effect of diamond scriber shape and friction coefficient on stresses and crack initiation. A number of scriber shapes including spherical tips with different radii, conical tips with different included angles and faceted tips such as Berkovich and Vickers were modeled and simulated.

Figure 10 shows the effects of scribing depth and friction coefficient for a spherical tipped scriber with a tip radius of 3 μm (similar to Scriber II presented earlier). It can be seen that a higher friction coefficient produces a larger tensile stress with increasing depth and a correspondingly smaller critical depth of cut for ductile-to-brittle transition. This implies that lowering the friction coefficient will delay crack initiation and hence promote ductile cutting, which yields a smooth crack-free surface. The frictionless case is presented here only for comparison and does not have practical significance.

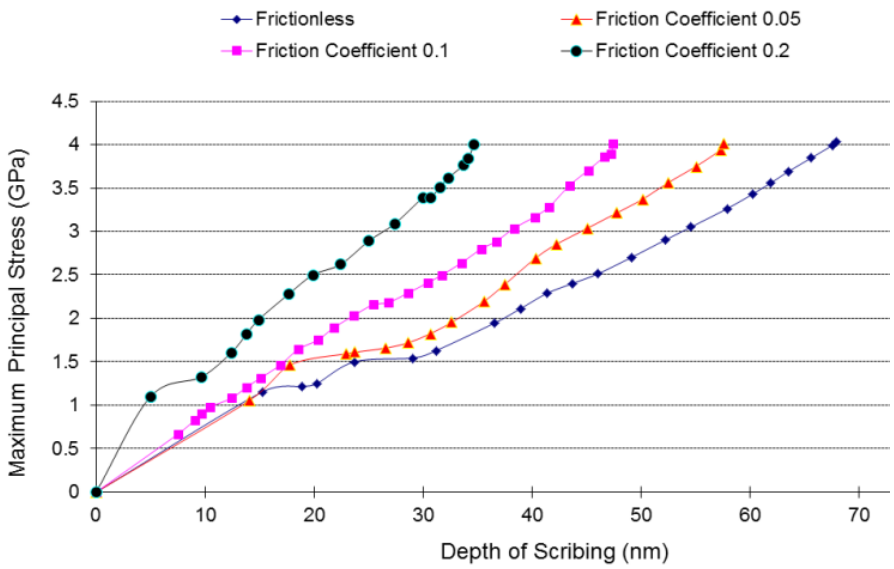

Figure 10. Effect of friction and scribing depth on stress evolution (spherical scriber with 3 μm tip radius).

Figure 11 shows the effect of scriber tip radius and friction coefficient on the critical depth of cut. It is clear that the critical depth is higher for a larger tip radius and lower friction coefficient. The higher critical depth is attributed to the large compressive stress field induced by the larger tip radius, which inhibits fracture initiation [7]. In all cases, the corresponding hydrostatic pressure for the crack initiation ranges from 9-15 GPa, which suggests material removal via ductile mode of cutting occurs prior to crack initiation.

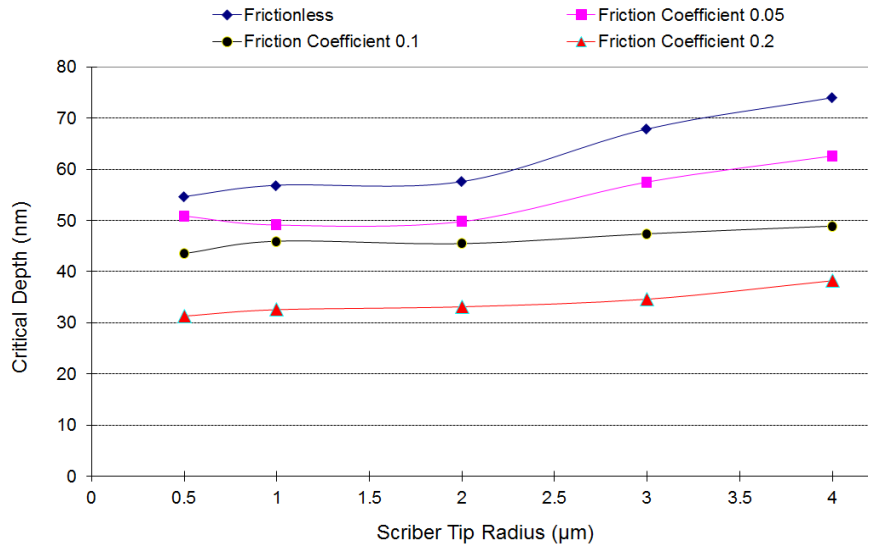

Figure 11. Effect of tip radius and friction on critical depth for spherical tips.

The effects of scribing depth and included angle of a sharp tipped (20 nm radius) conical scriber on the stresses and critical depth were also simulated. A friction coefficient of 0.05 was assumed. Figure 12 shows the effect of scribing depth on the subsurface stress contours for a 150° included angle scriber. It is seen that the maximum stress occurs under and slightly behind the scriber-silicon contact area. The sectional view reveals fairly high subsurface tensile stresses, whose distribution resembles the shape of median and/or lateral cracks that are known to occur in the subsurface for sharp indenters [25-26]. However, the subsurface tensile stress in the present case is insufficient (< 4GPa) to nucleate cracks, and as the scribing depth increases the maximum principal stress shifts to the surface and finally produces surface cracks.

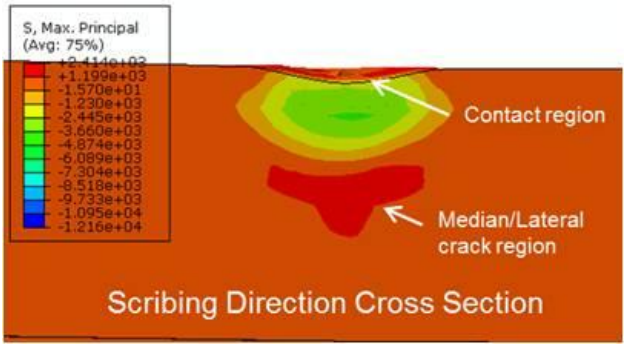

Figure 12. Subsurface stress contours (in a section normal to scribing direction) for a 150° conical tip and 2.6 nm scribing depth.

Figure 13 summarizes the effect of included angle on the stress and critical depth. It can be seen that the critical depth increases with the included angle. This is again due to the larger compressive stresses induced in the material, which delay crack initiation and inhibit their propagation. This is consistent with results reported elsewhere for diamond turning of brittle materials with large negative rake angle tools, which exhibit greater ductile mode cutting behavior [7-9,27]. The hydrostatic pressure corresponding to the critical depth ranges from 18-21 GPa, which suggests ductile mode of cutting dominates prior to material fracture.

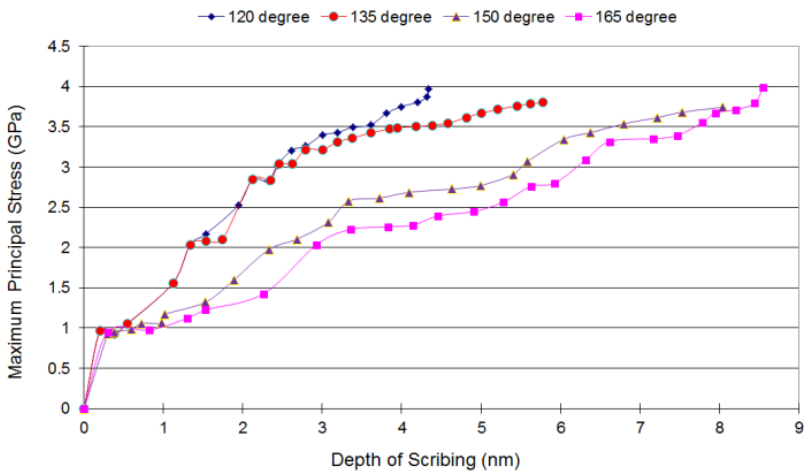

Figure 13. Effect of included angle and depth on stress for conical scriber.

Scribing by Berkovich and Vickers indenters was also studied to shed light on the cutting performance of faceted cutting grits due to their frequent appearance in diamond wires. Similar to the modeling of conical indenters presented earlier, all sharp edges in these scribers were rounded with 20 nm fillet radii and a friction coefficient of 0.05 was assumed.

It is found the stress distributions generated by the Berkovich and Vickers scribers exhibit the same features as the conical scriber. Namely, at a small depth of scribing the maximum principal stress is produced in the subsurface, and the orientation of the tensile stress suggests the possible generation of median/lateral cracks. At larger scribing depths, the maximum principal stress moves to the surface of the silicon wafer. While a large tensile stress region is still produced in the subsurface, cracks are first generated in the tensile stress region of the surface, as shown in Fig. 14.

Figures 14a and 14b show the geometry of scribing with the Berkovich tip. Figure 14a shows the scribing process with the edge of the Berkovich tip leading while Fig. 14b shows the face of the scriber tip leading. Note also that the Berkovich tip is modeled using shell elements instead of a solid body. It is interesting to note that the shape of the large tensile stress region and the crack formation paths are modified significantly if the tip is rotated 180

degrees around the vertical axis of the scriber (compare Figs. 14c and 14d). In both cases the large tensile stresses in the surface follow the scriber-silicon surface contact region, and the change in orientation of the scriber tip has led to a change in the stress field, and crack initiation and propagation. The critical depth of cut in both cases is 8.9 nm.

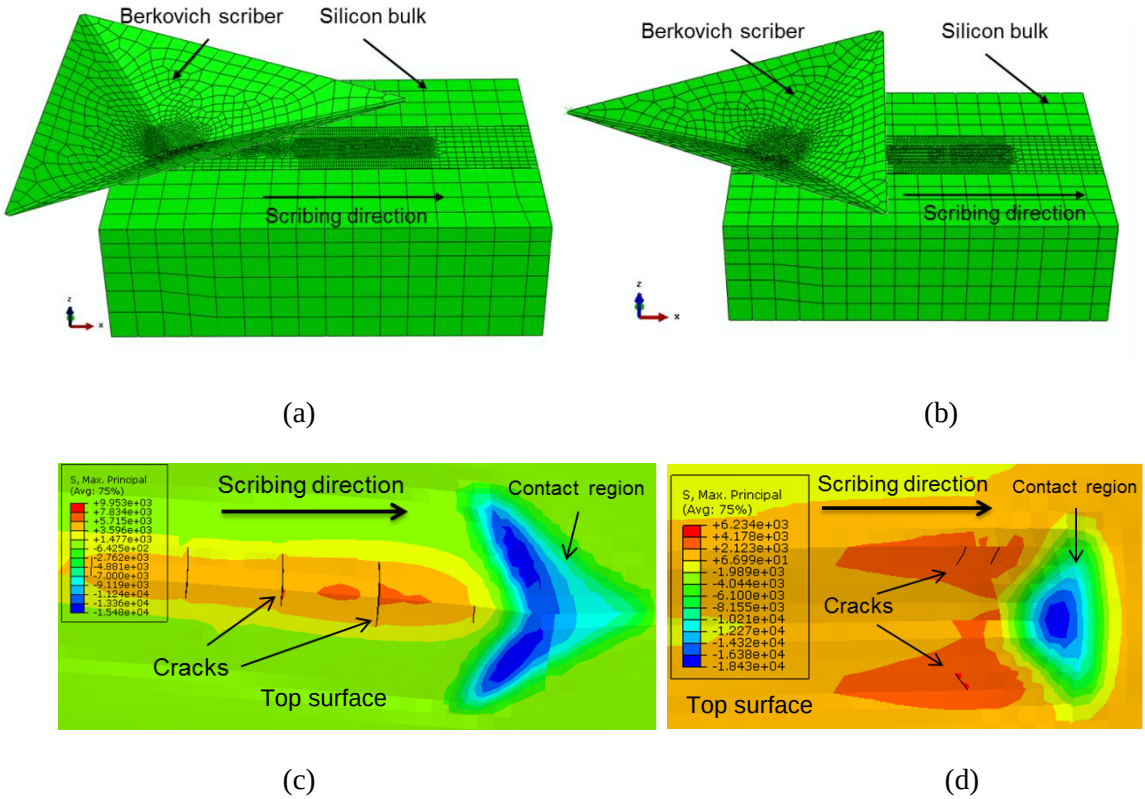

Figure 14. Stresses and cracks generated by Berkovich tip: edge leading (a & c) and face leading (b & d).

Similar patterns of stress distribution and crack generation are also observed for scribing with a Vickers tip (pyramidal tip with four facets). Scribing with one of the four edges of the scriber as the leading edge yields a critical depth of cut of 8.9 nm, while a slightly higher critical depth of 9.1 nm is obtained after a 45° rotation of the tip about its vertical axis. In both cases, the maximum tensile stresses occur in the subsurface and then shift to surface as the scribing depth increases and finally surface cracks form. The tensile stress in the subsurface

can be as large as 3.5 GPa. The two orientations of the scriber tip yield different maximum tensile stress distributions and crack propagation paths corresponding to the critical depths of cut for the two orientations. In actual sawing practice, due to the presence of microcracks, the fracture strength of c-Si may be lower than the 4 GPa fracture strength assumed in the XFEM model. If the fracture strength is less than 3.5 GPa, subsurface cracks can be initiated before the generation of surface cracks.

3.4 Effects of hydrostatic pressure on crack initiation

It is well known that the fracture strength of a brittle material is higher when subjected to external hydrostatic pressure [28]. Single grit scribing tests on silicon carried out in a chamber with 400 MPa hydrostatic pressure have shown that crack generation in the material can be delayed, thereby allowing ductile mode cutting to be carried out at a larger scribing depth [29]. To analyze this effect via the XFEM model, scribing of monocrystalline silicon with a spherical scriber of 3 μm tip radius under different hydrostatic pressures was simulated. The results show that, for a friction coefficient of 0.05, as the hydrostatic pressure increases from zero to 800 MPa in increments of 200 MPa, the critical depth for ductile-to-brittle transition increases from 57.5 nm to 60.6 nm, 62.1 nm, 64.1 nm and 67.1 nm, respectively. The stress evolution as a function of scribing depth and the magnitude of hydrostatic pressure is shown in Fig. 15. This agrees with experimental observations reported in literature [29].

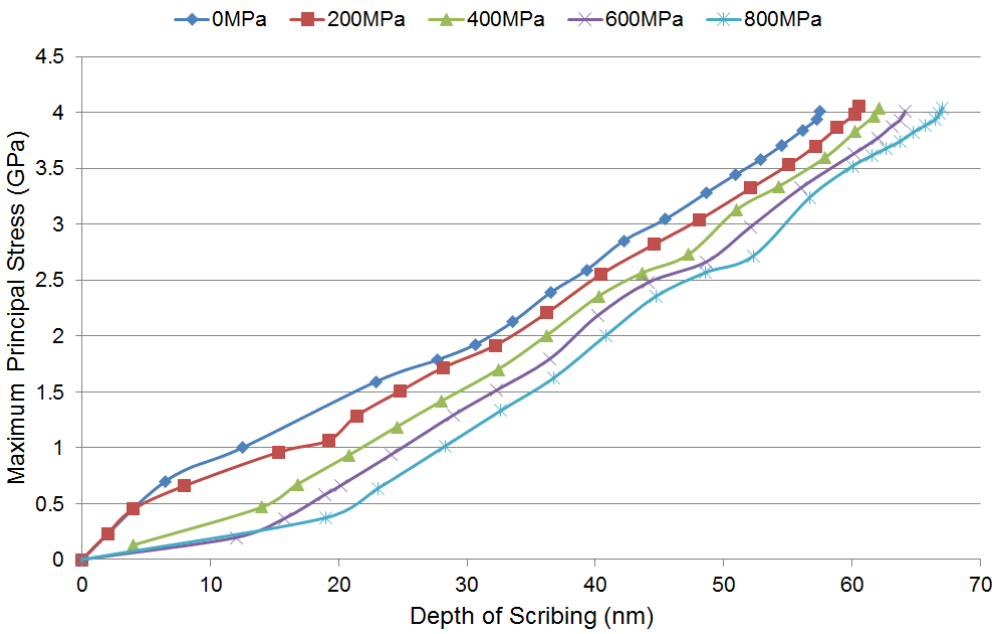

Figure 15. Effect of hydrostatic pressure and depth on stress for a spherical scriber (3 μm tip radius).

4 CONCLUSIONS

The paper modeled and analyzed the effects of abrasive shape, friction coefficient, and external hydrostatic pressure on the ductile-to-brittle transition in single grit diamond scribing of monocrystalline silicon. The work was motivated by the need for fundamental understanding of the factors affecting material removal and surface generation in fixed abrasive diamond wire sawing of PV silicon wafers. An XFEM model of the single grit scribing process was built and shown to yield predictions of the critical depth of cut for ductile-to-brittle transition for silicon that are in reasonable agreement with diamond scribing experiments.

The modeling results show that ductile mode cutting, which yields a smooth crack-free surface, can be induced by suitably controlling abrasive shape parameters such as the grit tip radius (for spherical abrasives) and included angle (for conical abrasives). Increasing the tip radius and/or the included angle increases the critical depth by delaying crack initiation in

silicon. In contrast to blunt tips (flat and spherical), which only initiate surface cracks at the dutile-to-brittle transition point, sharp tips (conical, Berkovich and Vickers) always generate large tensile stress regions in the subsurface, which can lead to the initiation of median and lateral cracks.

In addition, lowering the friction coefficient, e.g. by altering the cutting fluid properties in the actual wire sawing process, also yields a higher critical depth of cut. The model also correctly captures the increase in critical depth of cut with increasing hydrostatic pressure.

It is noted that a higher critical depth of cut implies the possibility of a higher feed rate in wire sawing without surface/subsurface cracking. These results are expected to be useful in optimizing the diamond wire and its application to wafering of PV silicon ingots.

5 REFERENCES

[1] Möller, H.J, Advanced Engineering Materials, 2004. 6 (7): p. 501-513.

[2] Möller, H.J, Physica Status Solidi (a), 2006. 203 (4): p. 659-669.

[3] Tso, P., et at, Material Science Forum, 2006. 505-507: p. 1219-1224.

[4] Bidiville, A., et al, Proceedings of the 24th EUPVSEC, 2009 Hamburg, p. 1400-1405.

[5] Bifano, T.G., Dow, T.A., Scattergood, R.O, Journal of Engineering for Industry, Transactions of the ASME, 1991. 113(2): p. 184-189.

[6] Scott, C.G and Danyluk, S., Wear, 1992. 152: p. 183-185.

[7] Li, X.P., et al., Interntional Journal of Advanced Manufacturing Technology, 2010. 48: p. 993-999

[8] Cai, M.B., Li, X.P., Rahman, M., Proc. IMechE, Part B: J Engineering Manufacture, 2007. 221(10): p. 1511-1519.

[9] Liu, K., et al., International Journal of Advanced Manufacturing Technology, 2007. 33: p. 875-884.

[10] Yan, J., et al., Precision Engineering, 2009. 33:378-386.

[11] Wang, J.J and Liao, Y.Y., Journal of Engineering Materials and Technology, 2008. 130: 011002.

[12] Shibata, T, et al., Precision Engineering, 1996. 18: p. 129-137.

[13] Shibata, T., et al., Applied Physics Letters, 1994. 65(20): p. 2553-2555.

[14] Gogotsi, Y., et. Al., Semiconductor Science and Technology, 2001. 16(5): p. 345-352.

[15] Morris, J.C., and Callahan, D.L., Journal of Material Research, 1994. 9 (11): p.2907-2913

[16] Moes, N. et al., International Journal of Numerical Methods in Engineering, 1999. 46: p. 131-150.

[17] Areias, P.M.A and Belytschko, T., International Journal of Numerical Methods in Engineering, 2005. 63: p. 760-788.

[18] ABAQUS Analysis User's Manual, Version 6.10.

[19] Hu, J.Z., et al., Physical Review B, 1986. 34: p. 4679 - 4684.

[20] Wortman, J.J and Evans, R.A., Journal of Aplied Physics, 1965. 36: p. 153-156.

[21] Duclos, S., Vohra, Y., Ruoff, A., Physical Review B, 1990. 41(17): p. 12021-12028.

[22] Gerbig, Y.B., et al., Journal of Material Research, 2009. 24(3): p. 1172-1182.

[23] Kozhushko, V.V., and Hess, P., Engineering Fracture Mechanics, 2010, (77): p. 193-200

[24] Hesketh, P.J., et al., Journal of Electrochemical Society, 1993. 140(4): p. 1080-1085.

[25] Marshall, D.B., et al, Journal of American Ceramic Society, 1982, 65(11): 561 – 566

[26] Lawn, B.R., et al, Journal of American Ceramic Society, 1980, 63(9-10): 574 – 581

[27] Fang, F.Z and Zhang, G.X., International Journal of Advanced Manufacturing Technology, 2003. 22: p. 703-707.

[28] Bridgman, P.W., Journal of Applied Physics, 1947. 18: p. 246-258.

[29] Yoshino, M., et al., Journal of Mechanical Sciences, 2001. 43: p. 335-347.